
MANO: Exploiting Matrix Norm for Unsupervised Accuracy Estimation Under Distribution Shifts

Renchunzi Xie*
NTU[†]

Ambroise Odonnat*
Huawei Noah’s Ark Lab

Vasilii Feofanov*
Huawei Noah’s Ark Lab

Weijian Deng
ANU[‡]

Jianfeng Zhang
Huawei Noah’s Ark Lab

Bo An
NTU[†]

Abstract

Leveraging the model’s outputs, specifically the logits, is a common approach to estimating the test accuracy of a pre-trained neural network on out-of-distribution (OOD) samples without requiring access to the corresponding ground-truth labels. Despite their ease of implementation and computational efficiency, current logit-based methods are vulnerable to overconfidence issues, leading to prediction bias, especially under the natural shift. In this work, we first study the relationship between logits and generalization performance from the view of low-density separation assumption. Our findings motivate our proposed method MANO that (1) applies a data-dependent normalization on the logits to reduce prediction bias, and (2) takes the L_p norm of the matrix of normalized logits as the estimation score. Our theoretical analysis highlights the connection between the provided score and the model’s uncertainty. We conduct an extensive empirical study on common unsupervised accuracy estimation benchmarks and demonstrate that MANO achieves state-of-the-art performance across various architectures in the presence of synthetic, natural, or subpopulation shifts.

1 Introduction

The deployment of machine learning models in real-world scenarios is frequently challenged by distribution shifts between the training and test data. These shifts can substantially deteriorate the model’s performance during testing (Geirhos et al., 2018; Koh et al., 2021; Quionero-Candela et al., 2009) and introduce significant risks related to AI safety (Deng and Zheng, 2021; Hendrycks and Mazeika, 2022). To alleviate this issue, it is common to monitor model performance by periodically collecting the ground truth labels for a subset of the current test dataset (Lu et al., 2023). However, this approach is often resource-intensive and time-consuming, which motivates the importance of estimating the model’s performance on out-of-distribution (OOD) data in an unsupervised manner, also known as *Unsupervised Accuracy Estimation* (Donmez et al., 2010).

Due to privacy constraints and computational efficiency, one of the most popular ways to estimate accuracy without labels is to rely on the model’s outputs, called logits, as a source of confidence in the model’s predictions (Deng et al., 2023; Garg et al., 2022; Guillory et al., 2021; Hendrycks and Gimpel, 2016). For instance, *ConfScore* (Hendrycks and Gimpel, 2016) leverages the average maximum softmax probability as the test accuracy estimator, while Deng et al. (2023) has recently proposed to estimate the accuracy via the nuclear norm of the softmax probability matrix. These approaches, however, tend to underperform on the natural shift applications while the intuition behind the use of logits remains unclear. This motivates us to ask:

* Equal contribution † Nanyang Technological University ‡ Australian National University

Question 1 *What explains the correlation between logits and generalization performance?*

In section 3, we show that logits are connected to the model’s margins, *i.e.*, the distances between the learned embeddings and the decision boundaries. Inspired by the low-density separation (LDS) assumption (Chapelle and Zien, 2005; Feofanov et al., 2023) that optimal decision boundaries should lie in low-density regions, we propose MANO, an estimation score that aggregates the margins at a dataset level by taking the L_p -norm of the normalized model’s prediction matrix to evaluate the density around decision boundaries. Nevertheless, logit-based approaches are known to suffer from overconfidence (Odonnat et al., 2024; Wei et al., 2022a), resulting in high prediction bias, especially under poorly-calibrated scenarios. This leads us to another critical question:

Question 2 *How to alleviate the overconfidence issues of logits-based methods?*

In section 4, we reveal that this question is connected to the normalization of logits and show that the widely-used softmax normalization accumulates errors in the presence of prediction bias, which can lead to overconfidence and significantly degrade the performance of existing accuracy estimation methods in poorly-calibrated scenarios. To mitigate this issue, we propose a novel normalization strategy called SoftTrun that takes into account the empirical distribution of logits and aims to find a trade-off between information completeness of ground-truth logits and error accumulation.

Summary of our contributions. (1) We show that logits are informative of generalization performance through the lens of the low-density separation assumption by reflecting the distances to decision boundaries. (2) We identify the failure of the commonly-used softmax normalization that accumulates errors under poorly calibrated because of its overconfidence, leading to biased estimation. (3) We propose MANO, a training-free estimation method that quantifies the global distances to decision boundaries by taking the L_p norm of the logits matrix. MANO relies on a novel normalization technique that makes a trade-off between information completeness and error accumulation and is robust to different calibration scenarios. In addition, we demonstrate its connection to the model’s uncertainty. (4) We demonstrate the superiority of MANO compared to 11 competitors with a large-scale empirical evaluation including 12 benchmarks across diverse distribution shifts. Results show that MANO consistently improves over the state-of-the-art baselines, including on the challenging natural shift.

2 Problem Statement

Setting. Consider a classification task with input space $\mathcal{X} \subset \mathbb{R}^D$ and label space $\mathcal{Y} = \{1, \dots, K\}$. Let p_S and p_T be the source and target distributions on $\mathcal{X} \times \mathcal{Y}$, respectively, with $p_S \neq p_T$. During pre-training, we train a neural network $f: \mathcal{X} \rightarrow \mathbb{R}^K$ on a training set $\mathcal{D}_{\text{train}}$ with samples drawn i.i.d. from p_S . The model can be parameterized as $f = f_{\mathbf{W}} \circ f_{\phi}$, where $f_{\phi}: \mathcal{X} \rightarrow \mathbb{R}^q$ is a feature extractor and $f_{\mathbf{W}}: \mathbb{R}^q \rightarrow \mathbb{R}^K$ is a linear classifier with parameters $\mathbf{W} = (\omega_k)_{k=1}^K \in \mathbb{R}^{q \times K}$. Further, we denote an input by \mathbf{x} , its corresponding label by y , its representation by $\mathbf{z} = f_{\phi}(\mathbf{x})$ and logits by $\mathbf{q} = f(\mathbf{x}) = (\omega_k^{\top} \mathbf{z})_k \in \mathbb{R}^K$. The test accuracy of f on \mathcal{D} is defined as $\text{Acc}(f, \mathcal{D}) := \frac{1}{|\mathcal{D}|} \sum_{(\mathbf{x}, y) \in \mathcal{D}} \mathbb{1}_{\hat{y}=y}$ with predicted labels \hat{y} . The probability simplex is denoted by $\Delta_K = \{\mathbf{p} \in [0, 1]^K \mid \mathbb{1}_K^{\top} \mathbf{p} = 1\}$.

Unsupervised accuracy estimation. Given a model f pre-trained on $\mathcal{D}_{\text{train}}$, the goal of *unsupervised accuracy estimation* is to assess the generalization performance of f on target data drawn from p_T without having access to ground-truth target labels. This is a challenging task as we are subject to distribution shifts, *i.e.* $p_S \neq p_T$, which often occur in real-world scenarios, and ground-truth labels are inaccessible which prevents monitoring the model generalization performance at test time. In practice, given an unlabeled test set $\mathcal{D}_{\text{test}} = \{\mathbf{x}_i\}_{i=1}^N$ with N samples drawn i.i.d. from p_T , we aim to provide an estimation score $\mathcal{S}(f, \mathcal{D}_{\text{test}})$ that exhibits a linear correlation with the true OOD accuracy $\text{Acc}(f, \mathcal{D}_{\text{test}})$. Following the standard closed-set setting, both p_T and p_S involve the same K classes. We refer the reader to Appendix B for an extended discussion of related work.

3 What Explains the Correlation between Logits and Test Accuracy?

Although existing literature has shown the feasibility of unsupervised accuracy prediction under distribution shift by utilizing the model’s logits (Deng et al., 2023; Garg et al., 2022; Guillory et al., 2021), the reason behind this empirical success remains unclear. In this section, we seek to understand

when and why logits can be informative for analyzing generalization performance. Based on the derived understanding, we propose our approach, MANO, for estimating generalization performance.

3.1 Motivation

Logits reflect the distances to decision boundaries. We analyze logits from a linear classification perspective in the embedding space, where the decision boundary of class k is the hyperplane $\{z' \in \mathbb{R}^q | \omega_k^\top z' = 0\}$. In Appendix D.4, we remind that the distance from a point \mathbf{z} to hyperplane ω_k is given by $d(\omega_k, \mathbf{z}) = |\omega_k^\top \mathbf{z}| / \|\omega_k\|$. As the pre-trained model is fixed and ω_k can be normalized, we derive that the logits in absolute values are proportional to the distance from the learned embeddings to the decision boundaries, *i.e.*, $|\mathbf{q}_k| = |\omega_k^\top \mathbf{z}| \propto d(\omega_k, \mathbf{z}), \forall k$. This indicates that the magnitude of logits reflects how close the corresponding embedding is from each decision boundary.

Low-density separation assumption.

When dealing with unlabeled data, it is required to make assumptions on the relationship between the distance to decision boundaries and generalization performance. The low-density separation assumption (LDS, Chapelle and Zien, 2005) states that optimal decision boundaries should lie in low-density regions (Figure 1) so that unlabeled margin $|\omega_k^\top \mathbf{z}|$ reflects reliable confidence in predicting \mathbf{x} to the class k . The assumption is often empirically supported as the misclassified samples tend to be significantly closer to the decision boundary than the correctly classified ones (Mickisch et al., 2020). This might indicate that **the absolute values of the logits are positively correlated to its generalization performance.**

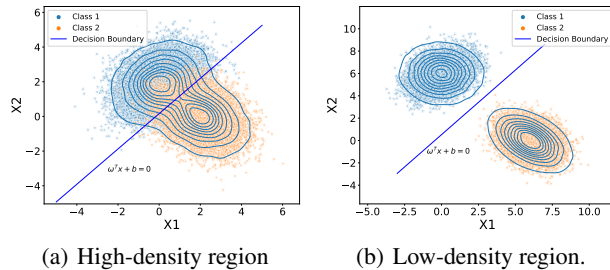


Figure 1: **Illustration of the LDS assumption.** When the boundary passes through dense regions (a), margins have little predictive power and can not be used without labels, while margins are informative in sparse regions (b).

Assumptions on the prediction bias. It is important to note that the LDS assumption has been initially proposed for semi-supervised learning, where labeled and unlabeled data are assumed to come from the same distribution, which is not the case in our setting. This leads to logits writing $f(\mathbf{x}) = \mathbf{q}^* + \varepsilon$ in the general case[‡], *i.e.*, subject to a potentially non-negligible prediction bias $\varepsilon = (\varepsilon_k)_k$ with respect to the ground-truth logits $\mathbf{q}^* \in \mathbb{R}^K$. The following proposition shows the impact of the prediction bias on the divergence between the true class posterior probabilities, assumed modeled as $\mathbf{p} = \text{softmax}(\mathbf{q}^*) \in \Delta_K$, and the estimated ones $\mathbf{s} = \text{softmax}(f(\mathbf{x})) \in \Delta_K$.

Proposition 3.1. *Let $\varepsilon_+ = (\max_l \{\varepsilon_l\} - \varepsilon_k)_k$. Then, the KL divergence between \mathbf{p} and \mathbf{s} verifies*

$$0 \leq \text{KL}(\mathbf{p} || \mathbf{s}) \leq \varepsilon_+^T \mathbf{p}.$$

The proposition indicates that a large approximation error of the posterior may be caused by prediction bias that has a large norm and/ or bad alignment with the true probabilities. Thus, the logit-based methods assume that the magnitude of the bias is reasonably bounded while the direction of bias does not drastically harm the ranking of classes by probabilities. We elaborate on this discussion and present the proof of Proposition 3.1 in Appendix D.1.

3.2 MANO: Predicting Generalization Performance With Matrix Norm of Logits

We have shown a connection between the feature-to-boundary distances and generalization performance as well as the impact of the prediction bias. Based on the derived intuition, we introduce MANO that leverages the model margins at the dataset level performing two steps: normalization and aggregation. The pseudo-code of MANO is provided in Appendix A.

[‡] We write this decomposition without loss of generality as no restrictions are imposed on ε .

Step 1: Normalization. Given that logits can exhibit significant variations in their scale depending on the input \mathbf{x} , it is crucial to normalize the logits within a standardized range to prevent outliers from exerting disproportionate influence on the estimation. A natural range stems from the fact that most deep classifiers have outputs in Δ_K , which amounts to applying a normalization function $\sigma: \mathbb{R}^K \rightarrow \Delta_K$ on top of the pre-trained neural network (Mensch et al., 2019), where Δ_K refers to probability simplex. This ensures having logits entries in $[0, 1]$. For each test sample \mathbf{x}_i , we first extract its learned feature representation $\mathbf{z}_i = f_\phi(\mathbf{x}_i)$. Then, logits corresponding to this representation are computed as $\mathbf{q}_i = f_{\mathbf{W}}(\mathbf{z}_i) \in \mathbb{R}^K$. The normalization procedure results in a prediction matrix $\mathbf{Q} \in \mathbb{R}^{N \times K}$ with each row \mathbf{Q}_i containing the normalized logits of an input sample:

$$\mathbf{Q}_i = \sigma(\mathbf{q}_i) \in \Delta_K, \quad (1)$$

where σ denotes the normalization function for the logits values. It is worth noting that not all normalization methods are appropriate candidates. The selection of a suitable normalization function σ based on different calibration scenarios will be discussed in detail in Section 4.

Step 2: Aggregation. Once the logits are scaled, we aggregate the dataset-level information on feature-to-boundary distances by taking the entry-wise L_p norm of the prediction matrix \mathbf{Q} , which can be expressed as:

$$\mathcal{S}(f, \mathcal{D}_{\text{test}}) = \frac{1}{\sqrt[p]{NK}} \|\mathbf{Q}\|_p = \left(\frac{1}{NK} \sum_{i=1}^N \sum_{k=1}^K |\sigma(\mathbf{q}_i)_k|^p \right)^{\frac{1}{p}}, \quad (2)$$

As we have $\|\mathbf{Q}\|_p \leq \sqrt[p]{NK} \max(\mathbf{Q}_{ij}) = \sqrt[p]{NK} (\mathbf{Q}_{ij} \in [0, 1])$, the scaling by $\sqrt[p]{NK}$ leads to $\mathcal{S}(f, \mathcal{D}_{\text{test}}) \in [0, 1]$, providing a standardized metric regardless of variations in the size of the test dataset N and the number of classes K . As p increases, MANO puts greater emphasis on high-margin terms, focusing on confident classification hyperplanes. In the extreme case where $p \rightarrow \infty$, we have $\|\mathbf{Q}\|_p \rightarrow \max(\mathbf{Q}_{ij})$. In practice, we choose $p = 4$ in all experiments and provide an ablation study on p in Appendix E.1. As the L_p norm is straightforward to compute, our approach is scalable and efficient compared to the current state-of-the-art method Nuclear (Deng et al., 2023) that requires performing a singular value decomposition.

3.3 Theoretical Analysis of MANO

In this section, we provide the theoretical support for the positive correlation between MANO and test accuracy. More specifically, we reveal that our proposed score is connected with the uncertainty of the neural network’s predictions in Theorem 3.3. Before presenting this result, we recall below the definition of Tsallis α -entropies introduced in Tsallis (1988).

Definition 3.2 (Tsallis α -entropies (Tsallis, 1988)). *Let $\alpha > 1$ and $k > 0$. The Tsallis α -entropy is defined as:*

$$\mathbf{H}_\alpha^T(\mathbf{p}) = k(\alpha - 1)^{-1}(1 - \|\mathbf{p}\|_\alpha^\alpha).$$

In this work, we choose $k = \frac{1}{\alpha}$ following Blondel et al. (2019). The Tsallis entropies generalize the Shannon entropy (limit case $\alpha \rightarrow 1$) and have been used in various applications (Blondel et al., 2019, 2020; Muzellec et al., 2017). More details can be found in Appendix C. The following theorem, whose proof is deferred to Appendix D.5, states that the estimation score obtained with MANO is a function of the averaged Tsallis entropy of the normalized neural network’s logits.

Theorem 3.3 (Connection to uncertainty). *Let $p > 1$, $a = \frac{p(p-1)}{K}$ and $b = \frac{1}{K}$. Given a test set $\mathcal{D}_{\text{test}} = \{\mathbf{x}_i\}_{i=1}^N$, corresponding logits $\mathbf{q}_i = f(\mathbf{x}_i)$, a normalization function $\sigma: \mathbb{R}^K \rightarrow \Delta_K$ and $p > 1$, the estimation score $\mathcal{S}(f, \mathcal{D}_{\text{test}})$ provided by MANO (Algorithm 1) verifies*

$$\mathcal{S}(f, \mathcal{D}_{\text{test}})^p = -a \left(\frac{1}{N} \sum_{i=1}^N \mathbf{H}_p^T(\sigma(\mathbf{q}_i)) \right) + b. \quad (3)$$

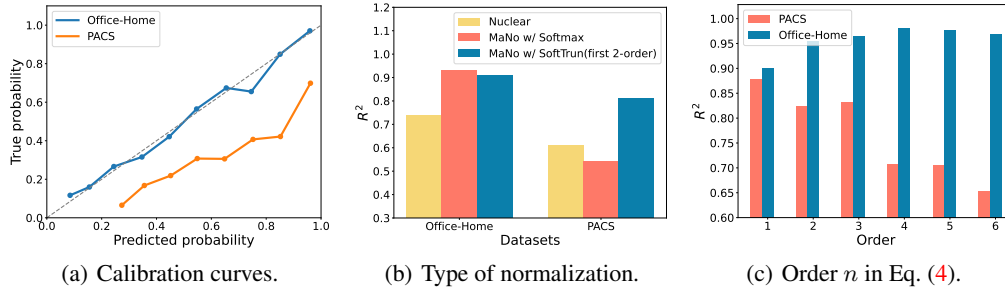


Figure 2: **Empirical evidence with Resnet18.** (a) The model is well-calibrated on Office-Home and miscalibrated on PACS. (b) `SoftTrun` is superior to the state-of-the-art `Nuclear` (Deng et al., 2023) in all scenarios while the `softmax` heavily fails on PACS. (c) Increasing the approximation order n in Eq. (4) is detrimental on PACS and beneficial on Office-Home. Taking $n \in \{2, 3\}$ is an optimal trade-off in all calibration scenarios.

As $a > 0$, Theorem 3.3 implies that the estimation score provided by MANO is negatively correlated with the average Tsallis-entropy on the test set. In particular, the less certain the model is on test data, the lower the test accuracy is and the higher the entropy term is in Eq. (3), resulting in a lower score $\mathcal{S}(f, \mathcal{D}_{\text{test}})$. As the converse sense holds, MANO provides a score positively correlated to the test accuracy. This follows the findings of Guillory et al. (2021); Wang et al. (2021) and empirically confirmed in Section 5 for various architectures, datasets, and types of shift.

4 How to Alleviate Overconfidence Issues of Logit-Based Methods?

The most common normalization technique of existing logit-based approaches is the `softmax` normalization. In this section, we show that the widely used `softmax` is sensitive to prediction bias, which hinders the quality of the estimation in poorly calibrated scenarios. To alleviate this issue, we propose a novel normalization strategy, `SoftTrun`, which balances the information completeness and overconfidence accumulation based on calibration.

4.1 The Failure of Softmax Normalization Under Poorly-Calibrated Scenarios

Empirical evidence. The `softmax` normalization can suffer from overconfidence issues (Odonnat et al., 2024; Wei et al., 2022b) and saturation of its outputs (Chen et al., 2017), with one entry close to one while the others are close to zero. Consequently, logit-based accuracy estimation methods using `softmax` are sensitive to prediction bias, leading to low-quality estimations in poorly calibrated scenarios. We illustrate this phenomenon in Figure 2(a) on two datasets, where a pre-trained ResNet18 exhibits more pronounced calibration issues on PACS (Li et al., 2017) compared to Office Home (Venkateswara et al., 2017). Figure 2(b) shows that using `softmax` in both MANO and the state-of-the-art method `Nuclear` (Deng et al., 2023) negatively impacts their accuracy estimation performance on the poorly calibrated PACS dataset.

Analysis. To alleviate those issues, we first notice that the `softmax` can be decomposed as $\text{softmax}(\mathbf{q}) = \exp(\mathbf{q}) / \sum_{k=1}^K \exp(\mathbf{q}_k) = (\phi \circ \exp)(\mathbf{q})$, where $\phi: \mathbb{R}_+^K \rightarrow \Delta_K$ writes $\phi(\mathbf{u}) = \mathbf{u} / \sum_{k=1}^K \mathbf{u}_k = \mathbf{u} / \|\mathbf{u}\|_1$. While ϕ has appealing property for normalization (see Proposition D.4), the exponential accumulates prediction errors, leading to the `softmax` overconfidence and a biased accuracy estimation. In particular, assume that the k -th entry of the output of the neural network on a test sample \mathbf{x}_i writes $\mathbf{q}_{i,k}^* + \varepsilon_k$, where $\mathbf{q}_{i,k}^*$ are the ground-truth logits and ε_k is the prediction error. Then, the n -order Taylor polynomial of the exponential writes

$$\exp(\mathbf{q}_{i,k}^* + \varepsilon_k) \approx 1 + (\mathbf{q}_{i,k}^* + \varepsilon_k) + \frac{(\mathbf{q}_{i,k}^* + \varepsilon_k)^2}{2!} + \dots + \frac{(\mathbf{q}_{i,k}^* + \varepsilon_k)^n}{n!}. \quad (4)$$

Figure 2(c) illustrates the impact of truncating Eq. (4) up to the n -th order. We conclude that a trade-off is needed between *information completeness on true logits* and *error accumulation* depending on the type of calibration scenario. Specifically, when the model is poorly calibrated on a given dataset

(*i.e.*, ε_k large in absolute value), the normalization should focus on avoiding error accumulation and when the model is well calibrated (*i.e.*, ε_k small in absolute value), the normalization should focus on information completeness.

4.2 SoftTrun: The Proposed Normalization Strategy

The above analysis shows that different calibration scenarios require an emphasis on different information during normalization. Therefore, we propose a normalization strategy called `SoftTrun` that normalizes the model outputs based on the calibration scenario. Given logits $\mathbf{q}_i \in \mathbb{R}^K$ and reusing the function ϕ previously introduced, it takes the general form:

$$\sigma(\mathbf{q}_i) = (\phi \circ v)(\mathbf{q}_i) = \frac{v(\mathbf{q}_i)}{\sum_{k=1}^K v(\mathbf{q}_i)_k} \in \Delta_K. \quad (5)$$

where $v: \mathbb{R}^K \rightarrow \mathbb{R}_+^K$ is designed to avoid error accumulation under poorly-calibrated scenarios by truncating the exponential ($n = 2$ in Eq. (4)) and using complete logits information under well-calibrated scenarios. As in practice, the calibration of the model on test data is unknown, `SoftTrun` employs a simple yet effective strategy reminiscent of pseudo-labeling (Lee, 2013; Sohn et al., 2020). More specifically, given a test dataset $\mathcal{D}_{\text{test}} = \{\mathbf{x}_i\}_{i=1}^N$ and corresponding logits $\mathbf{q}_i = f(\mathbf{x}_i)$, a criterion $\Phi(\mathcal{D}_{\text{test}})$ is computed at the dataset level and the normalized logits are defined as

$$v(\mathbf{q}_i) = \begin{cases} 1 + \mathbf{q}_i + \frac{\mathbf{q}_i^2}{2!}, & \text{if } \Phi(\mathcal{D}_{\text{test}}) \leq \eta \\ \exp(\mathbf{q}_i), & \text{if } \Phi(\mathcal{D}_{\text{test}}) > \eta \end{cases}. \quad (6)$$

We define $\Phi(\mathcal{D}_{\text{test}}) = -\frac{1}{NK} \sum_{j=1}^N \sum_{k=1}^K \log\left(\frac{\exp(\mathbf{q}_j)_k}{\sum_{j=1}^K \exp(\mathbf{q}_i)_j}\right)$, which is equal, up to a constant, to the average KL divergence between the uniform distribution and the predicted softmax probabilities. It follows from Tian et al. (2021) that showed that this KL divergence was small when the uncertainty of the model was high and large for confident models. Hence, when uncertainty is high, *i.e.*, $\Phi(\mathcal{D}_{\text{test}}) \leq \eta$, we truncate the exponential to reduce error accumulation, and when the model is certain, *i.e.*, $\Phi(\mathcal{D}_{\text{test}}) > \eta$, complete information is used with the exact exponential (and we recover the softmax). In all our experiments, we fix $\eta = 5$. In Appendix D, we provide theoretical insights on our choices of η and $\Phi(\mathcal{D}_{\text{test}})$ along with additional discussion.

5 Experiments

5.1 Experiment Setup

Pre-training datasets. For pre-training the neural network, we use a diverse set of datasets including CIFAR-10, CIFAR-100 (Krizhevsky and Hinton, 2009), TinyImageNet (Le and Yang, 2015), ImageNet (Deng et al., 2009), PACS (Li et al., 2017), Office-Home (Venkateswara et al., 2017), DomainNet (Peng et al., 2019) and RR1-WILDS (Taylor et al., 2019), and BREEDS (Santurkar et al., 2020) which leverages class hierarchy of ImageNet (Deng et al., 2009) to create 4 datasets including Living-17, Nonliving-26, Entity-13 and Entity-30.

Test datasets. In our comprehensive evaluation, we consider 12 datasets with 3 types of distribution shifts: the synthetic, the natural, and the subpopulation shifts. To verify the effectiveness of our method under the synthetic shift, we use CIFAR-10C, CIFAR-100C, and ImageNet-C (Hendrycks and Dietterich, 2019) that span 19 types of corruption across 5 severity levels, as well as TinyImageNet-C (Hendrycks and Dietterich, 2019) with 15 types of corruption and 5 severity levels. For the natural shift, we use the domains excluded from training from PACS, Office-Home, and DomainNet, RR1-WILDS as the OOD datasets. For the novel subpopulation shift, we consider the BREEDS benchmark with Living-17, Nonliving-26, Entity-13, and Entity-30 which are constructed from ImageNet-C.

Training details. To show the versatility of our method across different architectures, we perform experiments on ResNet18, ResNet50 (He et al., 2016), and WRN-50-2 (Zagoruyko and Komodakis, 2016) models. We train them for 20 epochs for CIFAR-10 (Krizhevsky and Hinton, 2009) and 50 epochs for the other datasets. In all cases, we use SGD with a learning rate of 10^{-3} , cosine learning rate decay (Loshchilov and Hutter, 2016), a momentum of 0.9, and a batch size of 128.

Table 1: Method comparison on four benchmarks with ResNet18, ResNet50 and WRN-50-2 under the **synthetic shift**, where R^2 refers to coefficients of determination, and ρ refers to the absolute value of Spearman correlation coefficients (higher is better). The best results are highlighted in **bold**. MANO consistently achieves the highest R^2 and ρ values across different datasets and network architectures, indicating its superior performance.

		Synthetic Shift																							
Dataset	Network	Rotation		ConfScore		Entropy		AgreeScore		ATC		Fréchet		Dispersion		ProjNorm		MDE		COT		Nuclear		MaNo	
		R^2	ρ	R^2	ρ	R^2	ρ	R^2	ρ	R^2	ρ	R^2	ρ	R^2	ρ	R^2	ρ	R^2	ρ	R^2	ρ	R^2	ρ	R^2	ρ
CIFAR 10	ResNet18	0.822	0.951	0.869	0.985	0.899	0.987	0.663	0.929	0.884	0.985	0.950	0.971	0.968	0.990	0.936	0.982	0.957	0.987	0.989	0.995	0.995	0.997	0.995	0.997
	ResNet50	0.835	0.961	0.935	0.993	0.945	0.994	0.835	0.985	0.946	0.994	0.858	0.964	0.987	0.990	0.944	0.989	0.978	0.963	0.984	0.996	0.994	0.996	0.996	0.997
	WRN-50-2	0.862	0.976	0.943	0.994	0.942	0.994	0.856	0.986	0.947	0.994	0.814	0.973	0.962	0.988	0.961	0.989	0.930	0.809	0.988	0.994	0.994	0.995	0.996	0.992
	Average	0.840	0.963	0.916	0.991	0.930	0.992	0.785	0.967	0.926	0.991	0.874	0.970	0.972	0.990	0.947	0.987	0.955	0.920	0.987	0.995	0.995	0.996	0.996	0.995
CIFAR 100	ResNet18	0.860	0.936	0.916	0.985	0.891	0.979	0.902	0.973	0.938	0.986	0.888	0.968	0.952	0.988	0.979	0.980	0.975	0.994	0.991	0.995	0.989	0.995	0.996	0.996
	ResNet50	0.908	0.962	0.919	0.984	0.884	0.977	0.922	0.982	0.921	0.984	0.837	0.972	0.951	0.985	0.988	0.991	0.988	0.995	0.985	0.996	0.979	0.994	0.995	0.997
	WRN-50-2	0.924	0.970	0.971	0.984	0.968	0.981	0.955	0.977	0.978	0.993	0.865	0.987	0.980	0.991	0.990	0.991	0.995	0.994	0.987	0.997	0.962	0.988	0.996	0.998
	Average	0.898	0.956	0.936	0.987	0.915	0.983	0.927	0.982	0.946	0.988	0.864	0.976	0.962	0.988	0.985	0.987	0.986	0.994	0.988	0.996	0.977	0.993	0.996	0.997
TinyImageNet	ResNet18	0.786	0.946	0.670	0.869	0.592	0.842	0.561	0.853	0.751	0.945	0.826	0.970	0.966	0.986	0.970	0.981	0.941	0.993	0.985	0.994	0.983	0.994	0.981	0.996
	ResNet50	0.786	0.947	0.670	0.869	0.651	0.892	0.560	0.853	0.751	0.945	0.826	0.971	0.977	0.986	0.979	0.987	0.941	0.993	0.980	0.994	0.965	0.994	0.980	0.996
	WRN-50-2	0.878	0.967	0.757	0.951	0.704	0.935	0.654	0.904	0.635	0.897	0.884	0.984	0.968	0.986	0.965	0.983	0.961	0.996	0.985	0.997	0.962	0.988	0.979	0.997
	Average	0.805	0.959	0.727	0.920	0.650	0.890	0.599	0.878	0.693	0.921	0.847	0.976	0.970	0.987	0.972	0.984	0.950	0.995	0.984	0.995	0.968	0.993	0.980	0.996
ImageNet	ResNet18	-	-	0.979	0.991	0.963	0.991	-	-	0.974	0.983	0.802	0.974	0.940	0.971	0.975	0.993	0.924	0.994	0.996	0.998	0.992	0.997	0.992	0.997
	ResNet50	-	-	0.980	0.994	0.967	0.992	-	-	0.970	0.983	0.855	0.974	0.938	0.968	0.986	0.993	0.886	0.994	0.993	0.996	0.985	0.997	0.991	0.998
	WRN-50-2	-	-	0.983	0.991	0.963	0.991	-	-	0.983	0.993	0.909	0.988	0.939	0.976	0.978	0.993	0.880	0.997	0.989	0.994	0.987	0.998	0.996	0.998
	Average	-	-	0.981	0.993	0.969	0.992	-	-	0.976	0.987	0.855	0.979	0.939	0.972	0.980	0.993	0.897	0.995	0.993	0.996	0.988	0.998	0.993	0.998

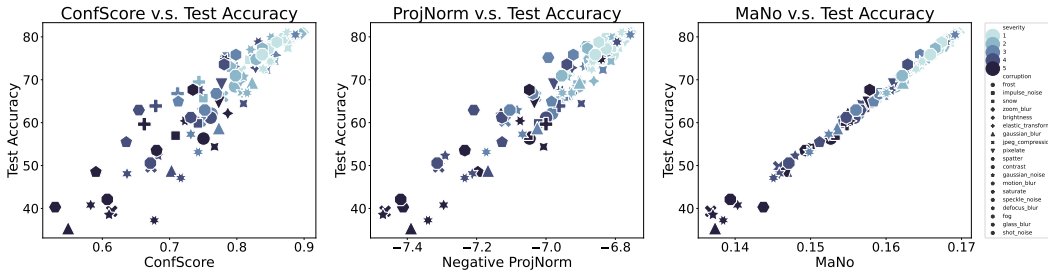


Figure 3: OOD error prediction versus True OOD error on Entity-13 with ResNet18. This scatter plot compares the performance of MANO with Dispersion Score and ProjNorm. Each point represents one dataset under a specific type and severity of corruption. Different shapes indicate different types of corruption, while darker colors indicate higher severity levels.

Evaluation Metrics We use the coefficient of determination (R^2 , Nagelkerke et al., 1991) and the Spearman’s rank correlation coefficient (ρ , Kendall, 1948) to evaluate performance. The ρ coefficient measures monotonicity, ranging from -1 to 1 , where values close to 1 or -1 indicate strong correlation, and 0 indicates no correlation. The R^2 coefficient measures the linearity and goodness of fit between estimates and accuracy, ranging from 0 to 1 , with 1 indicating a perfect fit.

Baselines. We consider 11 baselines commonly evaluated in the unsupervised accuracy estimation studies, including *Rotation Prediction* (Rotation) (Deng et al., 2021), *Averaged Confidence* (ConfScore) (Hendrycks and Gimpel, 2016), *Entropy* (Guillory et al., 2021), *Agreement Score* (AgreeScore) (Jiang et al., 2021), *Averaged Threshold Confidence* (ATC) (Garg et al., 2022), *AutoEval* (Fréchet) (Deng and Zheng, 2021), *ProjNorm* (Yu et al., 2022), *Dispersion Score* (Dispersion) (Xie et al., 2023), MDE (Peng et al., 2024), COT (Lu et al., 2024), and *Nuclear Norm* (Nuclear) (Deng et al., 2023).

5.2 Main Observations

MANO shows competitive performance gains under both synthetic and subpopulation shifts. Tables 1 and 2 present the numerical results of unsupervised accuracy estimation across 8 datasets using 3 different network architectures, evaluated under synthetic and subpopulation shifts. These shifts are quantified by R^2 and ρ . Empirical results demonstrate that these distribution shifts do not significantly impact calibration (*i.e.*, $S_{cali} \leq \eta$). We observe that MANO consistently outperforms other baselines, achieving state-of-the-art performance. For instance, MANO achieves $R^2 > 0.960$ and $\rho > 0.990$ under subpopulation shift, whereas the performance of other baselines does not reach such consistently high levels.

Table 2: Method comparison on four benchmarks using ResNet18, ResNet50, and WRN-50-2 under **subpopulation shift** with R^2 and ρ metrics (the higher the better). The best results are in **bold**.

		Subpopulation Shift																							
Dataset	Network	Rotation		ConfScore		Entropy		AgreeScore		ATC		Fréchet		Dispersion		ProjNorm		MDE		COT		Nuclear		MANo	
		R^2	ρ	R^2	ρ	R^2	ρ	R^2	ρ	R^2	ρ	R^2	ρ	R^2	ρ	R^2	ρ	R^2	ρ	R^2	ρ	R^2	ρ	R^2	ρ
Entity-13	ResNet18	0.927	0.961	0.795	0.940	0.794	0.935	0.543	0.919	0.823	0.945	0.950	0.981	0.937	0.968	0.952	0.981	0.927	0.995	0.960	0.985	0.978	0.991	0.992	0.996
	ResNet50	0.932	0.976	0.728	0.941	0.698	0.928	0.901	0.964	0.783	0.950	0.903	0.959	0.764	0.892	0.944	0.974	0.912	0.993	0.935	0.971	0.989	0.996	0.993	0.998
	WRN-50-2	0.939	0.983	0.930	0.977	0.919	0.973	0.871	0.935	0.936	0.980	0.906	0.958	0.815	0.905	0.950	0.977	0.925	0.995	0.944	0.979	0.989	0.995	0.992	0.996
	Average	0.933	0.973	0.817	0.953	0.804	0.945	0.772	0.939	0.847	0.958	0.920	0.966	0.948	0.977	0.839	0.922	0.921	0.995	0.947	0.979	0.985	0.994	0.993	0.996
Entity-30	ResNet18	0.964	0.979	0.570	0.836	0.553	0.832	0.542	0.935	0.611	0.845	0.849	0.978	0.929	0.968	0.952	0.987	0.931	0.994	0.971	0.993	0.980	0.993	0.991	0.996
	ResNet50	0.961	0.980	0.878	0.969	0.838	0.956	0.914	0.975	0.924	0.973	0.835	0.956	0.783	0.914	0.937	0.986	0.918	0.995	0.958	0.982	0.978	0.994	0.988	0.997
	WRN-50-2	0.940	0.978	0.897	0.974	0.878	0.970	0.826	0.955	0.936	0.984	0.927	0.973	0.927	0.973	0.959	0.986	0.925	0.995	0.944	0.979	0.985	0.996	0.988	0.997
	Average	0.955	0.978	0.781	0.926	0.756	0.919	0.728	0.956	0.823	0.934	0.871	0.969	0.880	0.952	0.949	0.987	0.925	0.995	0.970	0.988	0.981	0.994	0.989	0.996
Living-17	ResNet18	0.876	0.973	0.913	0.973	0.898	0.970	0.586	0.736	0.940	0.973	0.768	0.950	0.900	0.958	0.923	0.970	0.927	0.985	0.972	0.984	0.975	0.987	0.980	0.991
	ResNet50	0.906	0.956	0.880	0.967	0.853	0.961	0.633	0.802	0.938	0.976	0.771	0.926	0.851	0.929	0.903	0.924	0.914	0.985	0.953	0.973	0.967	0.976	0.975	0.997
	WRN-50-2	0.909	0.957	0.928	0.980	0.921	0.977	0.652	0.793	0.966	0.984	0.931	0.967	0.931	0.966	0.915	0.970	0.914	0.983	0.965	0.990	0.951	0.978	0.961	0.996
	Average	0.933	0.974	0.907	0.973	0.814	0.969	0.623	0.777	0.948	0.978	0.817	0.949	0.894	0.951	0.913	0.969	0.918	0.984	0.963	0.982	0.964	0.980	0.972	0.995
Nonliving-26	ResNet18	0.906	0.955	0.781	0.925	0.739	0.909	0.543	0.810	0.854	0.939	0.914	0.980	0.958	0.981	0.939	0.978	0.929	0.989	0.982	0.992	0.970	0.989	0.978	0.991
	ResNet50	0.916	0.970	0.832	0.942	0.776	0.918	0.638	0.837	0.893	0.960	0.848	0.950	0.805	0.907	0.873	0.972	0.907	0.993	0.962	0.984	0.956	0.985	0.975	0.995
	WRN-50-2	0.917	0.977	0.932	0.971	0.912	0.959	0.676	0.861	0.945	0.969	0.885	0.942	0.893	0.939	0.924	0.973	0.909	0.991	0.962	0.979	0.960	0.988	0.978	0.992
	Average	0.913	0.967	0.849	0.946	0.809	0.929	0.618	0.836	0.897	0.956	0.882	0.957	0.913	0.974	0.886	0.943	0.915	0.991	0.969	0.985	0.962	0.987	0.977	0.992

Table 3: Method comparison on four benchmarks with ResNet18, ResNet50 and WRN-50-2 under **natural shift** with R^2 and ρ metrics (the higher the better). The best results are highlighted in **bold**.

		Natural Shift																							
Dataset	Network	Rotation		ConfScore		Entropy		AgreeScore		ATC		Fréchet		Dispersion		ProjNorm		MDE		COT		Nuclear		MANo	
		R^2	ρ	R^2	ρ	R^2	ρ	R^2	ρ	R^2	ρ	R^2	ρ	R^2	ρ	R^2	ρ	R^2	ρ	R^2	ρ	R^2	ρ	R^2	ρ
PACS	ResNet18	0.822	0.895	0.594	0.755	0.624	0.755	0.613	0.832	0.514	0.650	0.624	0.804	0.832	0.825	0.161	0.419	0.003	0.153	0.790	0.783	0.609	0.874	0.827	0.909
	ResNet50	0.860	0.923	0.070	0.069	0.061	0.055	0.463	0.622	0.192	0.265	0.463	0.622	0.073	0.167	0.244	0.587	0.059	0.104	0.891	0.790	0.611	0.888	0.923	0.958
	WRN-50-2	0.865	0.902	0.646	0.678	0.629	0.671	0.377	0.858	0.752	0.832	0.558	0.832	0.111	0.167	0.474	0.650	0.072	0.244	0.890	0.888	0.607	0.867	0.924	0.972
	Average	0.849	0.906	0.437	0.501	0.438	0.494	0.488	0.770	0.486	0.582	0.548	0.337	0.338	0.275	0.293	0.552	0.045	0.065	0.857	0.820	0.609	0.876	0.891	0.946
Office-Home	ResNet18	0.822	0.930	0.795	0.909	0.761	0.881	0.054	0.146	0.571	0.615	0.605	0.755	0.453	0.664	0.064	0.202	0.331	0.650	0.863	0.874	0.692	0.783	0.926	0.930
	ResNet50	0.851	0.944	0.769	0.895	0.742	0.853	0.026	0.216	0.487	0.734	0.607	0.685	0.383	0.727	0.169	0.475	0.342	0.622	0.762	0.846	0.731	0.895	0.838	0.916
	WRN-50-2	0.823	0.958	0.741	0.874	0.696	0.846	0.132	0.405	0.383	0.643	0.589	0.706	0.456	0.713	0.172	0.531	0.342	0.650	0.863	0.874	0.766	0.874	0.800	0.895
	Average	0.832	0.944	0.768	0.892	0.733	0.860	0.071	0.256	0.480	0.664	0.601	0.715	0.431	0.702	0.135	0.403	0.339	0.650	0.781	0.855	0.730	0.850	0.854	0.913
DomainNet	ResNet18	0.568	0.692	0.670	0.736	0.423	0.609	0.326	0.668	0.429	0.597	0.704	0.903	0.202	0.516	0.219	0.443	0.358	0.445	0.897	0.910	0.758	0.789	0.902	0.937
	ResNet50	0.588	0.703	0.570	0.706	0.344	0.573	0.455	0.697	0.245	0.404	0.746	0.872	0.002	0.041	0.220	0.430	0.379	0.527	0.903	0.927	0.809	0.879	0.910	0.950
	WRN-50-2	0.609	0.712	0.774	0.874	0.711	0.845	0.437	0.698	0.846	0.918	0.585	0.831	0.003	0.034	0.363	0.466	0.520	0.713	0.885	0.935	0.850	0.911	0.893	0.978
	Average	0.588	0.702	0.671	0.722	0.493	0.676	0.406	0.688	0.507	0.639	0.678	0.869	0.069	0.197	0.234	0.446	0.419	0.562	0.894	0.919	0.805	0.895	0.899	0.949
RR1-WILDS	ResNet18	0.821	1.000	0.951	1.000	0.836	1.000	0.929	1.000	0.342	0.500	0.936	1.000	0.843	1.000	0.859	1.000	0.927	1.000	0.969	1.000	0.885	1.000	0.983	1.000
	ResNet50	0.740	1.000	0.918	1.000	0.819	1.000	0.938	1.000	0.986	1.000	0.935	1.000	0.737	1.000	0.867	1.000	0.938	1.000	0.960	1.000	0.906	1.000	0.978	1.000
	WRN-50-2	0.031	0.500	0.941	1.000	0.846	1.000	0.946	1.000	0.988	1.000	0.922	1.000	0.824	1.000	0.878	1.000	0.954	1.000	0.934	1.000	0.840	1.000	0.969	1.000
	Average	0.530	0.833	0.937	1.000	0.833	1.000	0.938	1.000	0.779	0.833	0.931	1.000	0.801	0.833	0.868	1.000	0.940	1.000	0.953	1.000	0.877	1.000	0.977	1.000

MANO with an appropriate normalization technique significantly boosts estimation performance under the natural shift. Table 3 illustrates the results of accuracy estimation under the natural shift on a total of four datasets. Since calibration performance affected by the natural shift is more complex than the other distribution shifts, we balance ground-truth logits and error accumulation via the value of $\Phi(\mathcal{D}_{\text{test}})$. From Table 3, we observe a significant improvement compared with the other benchmarks. For instance, our method achieves the best performance on all four datasets on average. To visualize the estimation performance, we provide the scatter plots for *Dispersion Score*, *ProjNorm* and MANO in Figure 3 on Entity-18 with ResNet18. We find that MANO presents a robust linear relationship between the designed scores and ground-truth OOD errors, while the other state-of-the-art baselines tend to exhibit a biased estimation of high test errors.

Robustness enhancement achieved by MANO. Figure 4 presents a box plot showing the estimation robustness across different distribution shifts on all datasets except ImageNet, using ResNet18. Results for ImageNet are excluded due to the lack of *Rotation* and *AgreeScore* data for this dataset, as these two methods require retraining the networks. We observe that the estimation performance of MANO is more stable than other baselines across three types of distribution shifts. Additionally, MANO achieves the highest median estimation performance.

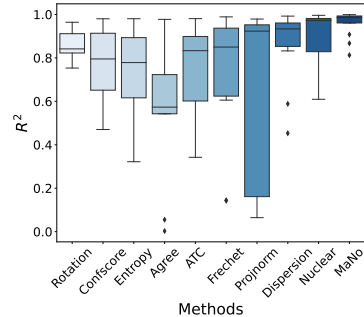


Figure 4: Robustness comparison between MANO and other baselines across three types of distribution shifts using ResNet18. MANO achieves the best and most robust overall estimations.

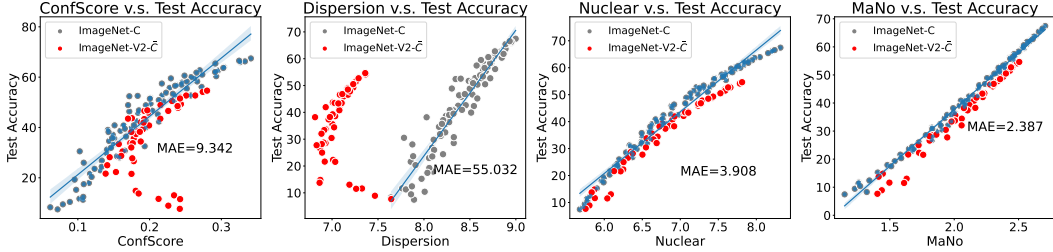


Figure 5: Comparison of generalization capability across four methods. Each subplot displays a linear regression model fitted on ImageNet-C, which is used to predict the accuracy on ImageNet-V2-C. The mean absolute error (MAE) is reported. All experiments are conducted using ResNet18.

5.3 Discussion

Generalization capabilities of MANO. To verify the generalization capabilities of MANO, we utilize designed scores calculated from ImageNet-C and their corresponding accuracy to fit a linear regression model. This model is then used to predict the test accuracy on ImageNet-V2-C, which is generated using the 10 new corruptions provided by (Mintun et al., 2021) on ImageNet-V2 (Recht et al., 2019). These new corruptions are perceptually dissimilar from those in ImageNet-C, including warps, blurs, color distortions, noise additions, and obscuring effects. Figure 5 shows that ConfScore and Dispersion give two distinct trends, while Nuclear exhibits some deviations for ImageNet-V2-C. In comparison, our MANO exhibits a consistent prediction pattern for both ImageNet-C and ImageNet-V2-C, aligning well with the linear regression model trained on ImageNet-C. Additionally, experimental results on ImageNet-C and ImageNet-C, generated from the validation set of ImageNet, are provided in Appendix E.4, further demonstrating the superiority of MANO.

Can SoftTrun enhance other logit-based methods? To study this, we conducted an ablation study by equipping SoftTrun with *Nuclear* (Deng et al., 2023), *ConfScore* (Hendrycks and Gimpel, 2016), and our MANO. In Table 4, we observe that SoftTrun significantly enhances the estimation performance R^2 of Nuclear. For example, Nuclear is improved from 0.692 to 0.826 on poorly-calibrated Office-Home.

Table 4: Effect of SoftTrun on other logit-based methods. SoftTrun significantly boosts the performance of Nuclear. The metric used is R^2 .

Dataset	ConfScore		MANO		Nuclear	
	w/o	w/	w/o	w/	w/o	w/
PACS	0.594	0.574	0.541	0.827	0.609	0.851
Office-Home	0.795	0.829	0.929	0.926	0.692	0.826

Limitations. Despite its soundness and strong empirical performance, our method has potential areas for improvement. One of these is the dependence on η in Eq. (6). In future work, we will explore a smoother way to automatically select the optimal normalization function without requiring hyperparameters. Additionally, if multiple validation sets are provided, as in (Deng et al., 2021; Deng and Zheng, 2021), we could select η based on those sets.

Ablation study. We provide an ablation studies on the L_p norm and Taylor order n in Appendix E.

6 Conclusion

In this paper, we introduce MANO, a simple yet effective training-free method to estimate test accuracy in an unsupervised manner using the Matrix Norm of neural network predictions on test data. Our approach is inspired by the LDS assumption that optimal decision boundaries should lie in low-density regions. To mitigate the negative impact of different distribution shifts on estimation performance, we first demonstrate the failure of softmax normalization under poor calibration, due to the accumulation of overconfident errors. We then propose a normalization strategy based on Taylor polynomial approximation, balancing logits information and error accumulation. Extensive experiments show that MANO consistently outperforms previous methods across various distribution shifts. This work highlights that logits imply the feature-to-boundary distance and considers the

impact of calibration on estimation performance. We hope our insights inspire future research to further explore the relationship between model outputs and generalization.

References

- Amini, M.-R., Feofanov, V., Pauletto, L., Hadjadj, L., Devijver, E., and Maximov, Y. (2022). Self-training: A survey. *arXiv preprint arXiv:2202.12040*.
- Bishop, C. M. (2006). *Pattern Recognition and Machine Learning*, page 738. Springer.
- Blondel, M., Martins, A., and Niculae, V. (2019). Learning classifiers with Fenchel-Young losses: Generalized entropies, margins, and algorithms. In Chaudhuri, K. and Sugiyama, M., editors, *Proceedings of the Twenty-Second International Conference on Artificial Intelligence and Statistics*, pages 606–615.
- Blondel, M., Martins, A. F. T., and Niculae, V. (2020). Learning with Fenchel-Young losses. *J. Mach. Learn. Res.*, 21(1).
- Chapelle, O. and Zien, A. (2005). Semi-supervised classification by low density separation. In *Proceedings of the Tenth International Workshop on Artificial Intelligence and Statistics*, pages 57–64.
- Chaudhari, P., Choromanska, A., Soatto, S., LeCun, Y., Baldassi, C., Borgs, C., Chayes, J., Sagun, L., and Zecchina, R. (2019). Entropy-SGD: Biasing gradient descent into wide valleys. *Journal of Statistical Mechanics: Theory and Experiment*, 2019(12):124018.
- Chen, B., Deng, W., and Du, J. (2017). Noisy softmax: Improving the generalization ability of dcnv via postponing the early softmax saturation. *2017 IEEE Conference on Computer Vision and Pattern Recognition (CVPR)*, pages 4021–4030.
- Chen, T., Kornblith, S., Norouzi, M., and Hinton, G. (2020). A simple framework for contrastive learning of visual representations. In *International Conference on Machine Learning*, pages 1597–1607.
- Choromanska, A., Henaff, M., Mathieu, M., Arous, G. B., and LeCun, Y. (2015). The loss surfaces of multilayer networks. In *Artificial Intelligence and Statistics*, pages 192–204.
- Croce, F. and Hein, M. (2020). Minimally distorted adversarial examples with a fast adaptive boundary attack. In *International Conference on Machine Learning*, pages 2196–2205.
- Dauphin, Y. N., Pascanu, R., Gulcehre, C., Cho, K., Ganguli, S., and Bengio, Y. (2014). Identifying and attacking the saddle point problem in high-dimensional non-convex optimization. *Advances in Neural Information Processing Systems*, 27.
- de Brébisson, A. and Vincent, P. (2016). An exploration of softmax alternatives belonging to the spherical loss family. In *International Conference on Learning Representations, (ICLR)*.
- Deng, J., Dong, W., Socher, R., Li, L.-J., Li, K., and Fei-Fei, L. (2009). ImageNet: A large-scale hierarchical image database. In *2009 IEEE Conference on Computer Vision and Pattern Recognition (CVPR)*, pages 248–255. Ieee.
- Deng, J., Guo, J., Xue, N., and Zafeiriou, S. (2019). ArcFace: Additive angular margin loss for deep face recognition. In *Proceedings of the IEEE/CVF Conference on Computer Vision and Pattern Recognition*, pages 4690–4699.
- Deng, W., Gould, S., and Zheng, L. (2021). What does rotation prediction tell us about classifier accuracy under varying testing environments? In *International Conference on Machine Learning (ICML)*, pages 2579–2589.
- Deng, W., Suh, Y., Gould, S., and Zheng, L. (2023). Confidence and dispersity speak: Characterising prediction matrix for unsupervised accuracy estimation. *arXiv preprint arXiv:2302.01094*.

- Deng, W. and Zheng, L. (2021). Are labels always necessary for classifier accuracy evaluation? In *Proceedings of the IEEE/CVF Conference on Computer Vision and Pattern Recognition (CVPR)*, pages 15069–15078.
- Dinh, L., Pascanu, R., Bengio, S., and Bengio, Y. (2017). Sharp minima can generalize for deep nets. In *International Conference on Machine Learning*, pages 1019–1028.
- Dohmatob, E. (2020). Distance from a point to a hyperplane. <https://math.stackexchange.com/questions/1210545/distance-from-a-point-to-a-hyperplane>.
- Donmez, P., Lebanon, G., and Balasubramanian, K. (2010). Unsupervised supervised learning i: Estimating classification and regression errors without labels. *Journal of Machine Learning Research*, 11(4).
- Fan, X., Wang, Q., Ke, J., Yang, F., Gong, B., and Zhou, M. (2021). Adversarially adaptive normalization for single domain generalization. In *Proceedings of the IEEE/CVF Conference on Computer Vision and Pattern Recognition*, pages 8208–8217.
- Fawzi, A., Moosavi-Dezfooli, S.-M., Frossard, P., and Soatto, S. (2018). Empirical study of the topology and geometry of deep networks. In *Proceedings of the IEEE Conference on Computer Vision and Pattern Recognition*, pages 3762–3770.
- Feofanov, V., Tiomoko, M., and Virmaux, A. (2023). Random matrix analysis to balance between supervised and unsupervised learning under the low density separation assumption. In *Proceedings of the 40th International Conference on Machine Learning*, pages 10008–10033.
- Freeman, C. D. and Bruna, J. (2016). Topology and geometry of half-rectified network optimization. *arXiv preprint arXiv:1611.01540*.
- Garg, S., Balakrishnan, S., Lipton, Z. C., Neyshabur, B., and Sedghi, H. (2022). Leveraging unlabeled data to predict out-of-distribution performance. *arXiv preprint arXiv:2201.04234*.
- Geirhos, R., Rubisch, P., Michaelis, C., Bethge, M., Wichmann, F. A., and Brendel, W. (2018). ImageNet-trained CNNs are biased towards texture; increasing shape bias improves accuracy and robustness. *arXiv preprint arXiv:1811.12231*.
- Gell-Mann, M. and Tsallis, C. (2004). *Nonextensive Entropy: Interdisciplinary Applications*.
- Gini, C. (1912). *Variabilità e mutabilità: contributo allo studio delle distribuzioni e delle relazioni statistiche. [Fasc. I.]*. Studi economico-giuridici pubblicati per cura della facoltà di Giurisprudenza della R. Università di Cagliari. Tipogr. di P. Cuppini.
- Guillory, D., Shankar, V., Ebrahimi, S., Darrell, T., and Schmidt, L. (2021). Predicting with confidence on unseen distributions. In *Proceedings of the IEEE/CVF international Conference on Computer Vision (ICCV)*, pages 1134–1144.
- He, K., Zhang, X., Ren, S., and Sun, J. (2016). Deep residual learning for image recognition. In *Proceedings of the IEEE Conference on Computer Vision and Pattern Recognition (CVPR)*, pages 770–778.
- He, W., Li, B., and Song, D. (2018). Decision boundary analysis of adversarial examples. In *International Conference on Learning Representations*.
- Hendrycks, D. and Dietterich, T. (2019). Benchmarking neural network robustness to common corruptions and perturbations. *arXiv preprint arXiv:1903.12261*.
- Hendrycks, D. and Gimpel, K. (2016). A baseline for detecting misclassified and out-of-distribution examples in neural networks. *arXiv preprint arXiv:1610.02136*.
- Hendrycks, D. and Mazeika, M. (2022). X-risk analysis for ai research. *arXiv preprint arXiv:2206.05862*.
- Heo, B., Lee, M., Yun, S., and Choi, J. Y. (2019). Knowledge distillation with adversarial samples supporting decision boundary. In *Proceedings of the AAAI conference on artificial intelligence*, volume 33, pages 3771–3778.

- Jiang, Y., Nagarajan, V., Baek, C., and Kolter, J. Z. (2021). Assessing generalization of SGD via disagreement. *arXiv preprint arXiv:2106.13799*.
- Karimi, H., Derr, T., and Tang, J. (2019). Characterizing the decision boundary of deep neural networks. *arXiv preprint arXiv:1912.11460*.
- Kendall, M. G. (1948). Rank correlation methods. *Michigan University*.
- Koh, P. W., Sagawa, S., Marklund, H., Xie, S. M., Zhang, M., Balsubramani, A., Hu, W., Yasunaga, M., Phillips, R. L., Gao, I., et al. (2021). Wilds: A benchmark of in-the-wild distribution shifts. In *International Conference on Machine Learning*, pages 5637–5664.
- Krizhevsky, A. and Hinton, G. (2009). Learning multiple layers of features from tiny images. *Technical Report*.
- Le, Y. and Yang, X. (2015). Tiny ImageNet visual recognition challenge. *CS 231N*, 7(7):3.
- Lee, D., Yu, S., and Yu, H. (2020). Multi-class data description for out-of-distribution detection. In *Proceedings of the 26th ACM SIGKDD International Conference on Knowledge Discovery & Data Mining*, pages 1362–1370.
- Lee, D.-H. (2013). Pseudo-Label : The Simple and Efficient Semi-Supervised Learning Method for Deep Neural Networks. *ICML 2013 Workshop : Challenges in Representation Learning (WREPL)*.
- Li, D., Yang, Y., Song, Y.-Z., and Hospedales, T. M. (2017). Deeper, broader and artier domain generalization. In *Proceedings of the IEEE international Conference on Computer Vision*, pages 5542–5550.
- Li, J., Shen, C., Kong, L., Wang, D., Xia, M., and Zhu, Z. (2022). A new adversarial domain generalization network based on class boundary feature detection for bearing fault diagnosis. *IEEE Transactions on Instrumentation and Measurement*, 71:1–9.
- Li, Y., Ding, L., and Gao, X. (2018). On the decision boundary of deep neural networks. *arXiv preprint arXiv:1808.05385*.
- Liu, W., Wen, Y., Yu, Z., Li, M., Raj, B., and Song, L. (2017). Sphereface: Deep hypersphere embedding for face recognition. In *Proceedings of the IEEE Conference on Computer Vision and Pattern Recognition*, pages 212–220.
- Loshchilov, I. and Hutter, F. (2016). SGDR: Stochastic gradient descent with warm restarts. *arXiv preprint arXiv:1608.03983*.
- Lu, Y., Qin, Y., Zhai, R., Shen, A., Chen, K., Wang, Z., Kolouri, S., Stepputtis, S., Campbell, J., and Sycara, K. (2023). Characterizing out-of-distribution error via optimal transport. *arXiv preprint arXiv:2305.15640*.
- Lu, Y., Qin, Y., Zhai, R., Shen, A., Chen, K., Wang, Z., Kolouri, S., Stepputtis, S., Campbell, J., and Sycara, K. (2024). Characterizing out-of-distribution error via optimal transport. *Advances in Neural Information Processing Systems*, 36.
- Madani, O., Pennock, D., and Flake, G. (2004). Co-validation: Using model disagreement on unlabeled data to validate classification algorithms. *Advances in Neural Information Processing Systems (NeurIPS)*, 17.
- Mensch, A., Blondel, M., and Peyré, G. (2019). Geometric losses for distributional learning. In *Proceedings of the 36th International Conference on Machine Learning*, pages 4516–4525.
- Mickisch, D., Assion, F., Greßner, F., Günther, W., and Motta, M. (2020). Understanding the decision boundary of deep neural networks: An empirical study. *arXiv preprint arXiv:2002.01810*.
- Mintun, E., Kirillov, A., and Xie, S. (2021). On interaction between augmentations and corruptions in natural corruption robustness. *Advances in Neural Information Processing Systems*, 34:3571–3583.
- Montufar, G. F., Pascanu, R., Cho, K., and Bengio, Y. (2014). On the number of linear regions of deep neural networks. *Advances in Neural Information Processing Systems*, 27.

- Muzellec, B., Nock, R., Patrini, G., and Nielsen, F. (2017). Tsallis regularized optimal transport and ecological inference. In *Proceedings of the Thirty-First AAAI Conference on Artificial Intelligence*, AAAI’17, page 2387–2393.
- Nagelkerke, N. J. et al. (1991). A note on a general definition of the coefficient of determination. *Biometrika*, 78(3):691–692.
- Negrinho, R. and Martins, A. (2014). Orbit regularization. In Ghahramani, Z., Welling, M., Cortes, C., Lawrence, N., and Weinberger, K., editors, *Advances in Neural Information Processing Systems*, volume 27.
- Odonnat, A., Feofanov, V., and Redko, I. (2024). Leveraging ensemble diversity for robust self-training in the presence of sample selection bias. In Dasgupta, S., Mandt, S., and Li, Y., editors, *Proceedings of The 27th International Conference on Artificial Intelligence and Statistics*, volume 238 of *Proceedings of Machine Learning Research*, pages 595–603. PMLR.
- Oord, A. v. d., Li, Y., and Vinyals, O. (2018). Representation learning with contrastive predictive coding. *arXiv preprint arXiv:1807.03748*.
- Peng, R., Zou, H., Wang, H., Zeng, Y., Huang, Z., and Zhao, J. (2024). Energy-based automated model evaluation. *arXiv preprint arXiv:2401.12689*.
- Peng, X., Bai, Q., Xia, X., Huang, Z., Saenko, K., and Wang, B. (2019). Moment matching for multi-source domain adaptation. In *Proceedings of the IEEE/CVF international Conference on Computer Vision*, pages 1406–1415.
- Peters, B., Niculae, V., and Martins, A. F. T. (2019). Sparse sequence-to-sequence models. In Korhonen, A., Traum, D., and Màrquez, L., editors, *Proceedings of the 57th Annual Meeting of the Association for Computational Linguistics*, pages 1504–1519.
- Platanios, E., Poon, H., Mitchell, T. M., and Horvitz, E. J. (2017). Estimating accuracy from unlabeled data: A probabilistic logic approach. *Advances in Neural Information Processing Systems (NeurIPS)*, 30.
- Platanios, E. A., Dubey, A., and Mitchell, T. (2016). Estimating accuracy from unlabeled data: A bayesian approach. In *International Conference on Machine Learning (ICML)*, pages 1416–1425.
- Poole, B., Lahiri, S., Raghu, M., Sohl-Dickstein, J., and Ganguli, S. (2016). Exponential expressivity in deep neural networks through transient chaos. *Advances in Neural Information Processing Systems*, 29.
- Quionero-Candela, J., Sugiyama, M., Schwaighofer, A., and Lawrence, N. D. (2009). *Dataset Shift in Machine Learning*. The MIT Press.
- Ranjan, R., Castillo, C. D., and Chellappa, R. (2017). L2-constrained softmax loss for discriminative face verification. *arXiv preprint arXiv:1703.09507*.
- Recht, B., Roelofs, R., Schmidt, L., and Shankar, V. (2019). Do imagenet classifiers generalize to imagenet? In *International Conference on Machine Learning*, pages 5389–5400.
- Santurkar, S., Tsipras, D., and Madry, A. (2020). Breeds: Benchmarks for subpopulation shift. *arXiv preprint arXiv:2008.04859*.
- Seldin, Y. and Tishby, N. (2010). Pac-bayesian analysis of co-clustering and beyond. *Journal of Machine Learning Research*, 11(117):3595–3646.
- Seo, S., Suh, Y., Kim, D., Kim, G., Han, J., and Han, B. (2020). Learning to optimize domain specific normalization for domain generalization. In *Computer Vision—ECCV 2020: 16th European Conference, Glasgow, UK, August 23–28, 2020, Proceedings, Part XXII 16*, pages 68–83. Springer.
- Sneddon, R. (2007). The Tsallis entropy of natural information. *Physica A: Statistical Mechanics and its Applications*, 386(1):101–118.
- Sohn, K. (2016). Improved deep metric learning with multi-class n-pair loss objective. *Advances in Neural Information Processing Systems*, 29.

- Sohn, K., Berthelot, D., Li, C.-L., Zhang, Z., Carlini, N., Cubuk, E. D., Kurakin, A., Zhang, H., and Raffel, C. (2020). Fixmatch: simplifying semi-supervised learning with consistency and confidence. In *Proceedings of the 34th International Conference on Neural Information Processing Systems*.
- Taylor, J., Earnshaw, B., Mabey, B., Victors, M., and Yosinski, J. (2019). Rxxr1: An image set for cellular morphological variation across many experimental batches. In *International Conference on Learning Representations (ICLR)*.
- Teimoori, Z., Rezazadeh, K., and Rostami, A. (2024). Inflation based on the Tsallis entropy. *The European Physical Journal C*, 84(1):80.
- Tian, J., Hsu, Y.-C., Shen, Y., Jin, H., and Kira, Z. (2021). Exploring covariate and concept shift for out-of-distribution detection. In *NeurIPS 2021 Workshop on Distribution Shifts: Connecting Methods and Applications*.
- Tsallis, C. (1988). Possible generalization of Boltzmann-Gibbs statistics. *Journal of Statistical Physics*, 52(1):479–487.
- Venkateswara, H., Eusebio, J., Chakraborty, S., and Panchanathan, S. (2017). Deep hashing network for unsupervised domain adaptation. In *Proceedings of the IEEE Conference on Computer Vision and Pattern Recognition (CVPR)*, pages 5018–5027.
- Wang, D., Shelhamer, E., Liu, S., Olshausen, B., and Darrell, T. (2021). Tent: Fully test-time adaptation by entropy minimization. In *International Conference on Learning Representations*.
- Wang, F., Xiang, X., Cheng, J., and Yuille, A. L. (2017). Normface: L2 hypersphere embedding for face verification. In *Proceedings of the 25th ACM international conference on Multimedia*, pages 1041–1049.
- Wei, H., Xie, R., Cheng, H., Feng, L., An, B., and Li, Y. (2022a). Mitigating neural network overconfidence with logit normalization. *arXiv preprint arXiv:2205.09310*.
- Wei, H., Xie, R., Cheng, H., Feng, L., An, B., and Li, Y. (2022b). Mitigating neural network overconfidence with logit normalization. In *Proceedings of the 39th International Conference on Machine Learning*, pages 23631–23644.
- Wu, Z., Xiong, Y., Yu, S. X., and Lin, D. (2018). Unsupervised feature learning via non-parametric instance discrimination. In *Proceedings of the IEEE Conference on Computer Vision and Pattern Recognition*, pages 3733–3742.
- Xie, R., Wei, H., Cao, Y., Feng, L., and An, B. (2023). On the importance of feature separability in predicting out-of-distribution error. *arXiv preprint arXiv:2303.15488*.
- Yousefzadeh, R. (2021). Deep learning generalization and the convex hull of training sets. *arXiv preprint arXiv:2101.09849*.
- Yu, Y., Yang, Z., Wei, A., Ma, Y., and Steinhardt, J. (2022). Predicting out-of-distribution error with the projection norm. *arXiv preprint arXiv:2202.05834*.
- Zagoruyko, S. and Komodakis, N. (2016). Wide residual networks. In *British Machine Vision Conference (BMVC)*.
- Zhang, X., Zhao, R., Qiao, Y., Wang, X., and Li, H. (2019). Adacos: Adaptively scaling cosine logits for effectively learning deep face representations. In *Proceedings of the IEEE/CVF Conference on Computer Vision and Pattern Recognition*, pages 10823–10832.

Appendix

Roadmap. In this appendix, we provide the pseudo-code of MANO in Section A. We discuss related work in Section B and provide some background on Tsallis entropies in Section C. Additional discussion and theoretical insights into Section 3.1 and Section 4 are given in Section D along with the proofs of the main results. Finally, we conduct a thorough ablation study and sensitivity analysis in Section E. We display the corresponding table of contents below.

Table of Contents

A Pseudo-Code of MANO	16
B Related Work	16
C Background on Tsallis Entropies	17
D Theoretical Insights and Proofs	17
D.1 Impact of Prediction Errors	17
D.2 Choice of Threshold $\Phi(\mathcal{D}_{\text{test}})$ in Eq. (6)	19
D.3 Choice of η in Eq. (6)	21
D.4 Distance to the Hyperplane	21
D.5 Proof of Theorem 3.3	22
D.6 Properties of ϕ	22
E Sensitivity Analysis and Ablation Study	23
E.1 Choice of L_p Norm.	23
E.2 Choice of Taylor Approximation order.	23
E.3 Superiority of SoftTrun.	23
E.4 Generalization Capabilities of MANO on ImageNet- \bar{C}	24

A Pseudo-Code of MANO

Algorithm 1 summarizes MANO introduced in Section 3.2, which is a lightweight, training-free method for unsupervised accuracy estimation using the neural network’s outputs.

Algorithm 1: Our proposed algorithm, MANO, for unsupervised accuracy estimation.

Input: Model f pre-trained on $\mathcal{D}_{\text{train}}$, test dataset $\mathcal{D}_{\text{test}} = \{\mathbf{x}_i\}_{i=1}^N$.

Parameters: Hyperparameter $p > 1$.

Initialization: Empty prediction matrix $\mathbf{Q} \in \mathbb{R}^{N \times K}$.

Criterion: compute threshold $\Phi(\mathcal{D}_{\text{test}})$ and choose σ following Eq. (6).

for $i \in \llbracket 1, N \rrbracket$ **do**

Inference: recover logits $\mathbf{q}_i = f(\mathbf{x}_i) \in \mathbb{R}^K$.

Normalization: obtain normalized logits $\sigma(\mathbf{q}_i) \in \Delta_K$.

Update: fill the prediction matrix $\mathbf{Q}_i \leftarrow \sigma(\mathbf{q}_i)$ following Eq. (1).

end

Output Estimation score $\mathcal{S}(f, \mathcal{D}_{\text{test}}) = \frac{1}{\sqrt[p]{NK}} \|\mathbf{Q}\|_p$ following Eq. (2).

B Related Work

Unsupervised accuracy estimation. This task aims to estimate model generalization performance on unlabeled test sets. To achieve this, several directions have been proposed. (1) Utilizing model outputs: One popular research direction is to use the model outputs on distribution-shifted data to construct a linear relationship with the test accuracy (Deng et al., 2023; Garg et al., 2022; Guillory et al., 2021; Hendrycks and Gimpel, 2016). For example, a recent work (Deng et al., 2023) introduced the nuclear norm of the softmax probability matrix as the accuracy estimator. However, current approaches following this direction significantly suffer from the overconfidence issues (Wei et al., 2022a), leading to fluctuating estimation performance across natural distribution shifts. Our work focuses on addressing this issue by balancing logit-information completeness and overconfidence-information accumulation. (2) Considering distribution discrepancy: another direction examines the negative relation between test accuracy and the distribution discrepancy between the training and test datasets (Deng and Zheng, 2021; Lu et al., 2023; Yu et al., 2022). However, commonly-used distribution distances do not guarantee stable accuracy estimation under different distribution shifts (Guillory et al., 2021; Xie et al., 2023), and some of these methods are time-consuming on large-scale datasets due to the requirement of training data (Deng and Zheng, 2021). (3) Constructing unsupervised losses: methods such as data augmentation and multiple-classifier agreement have also been introduced (Jiang et al., 2021; Madani et al., 2004; Platanios et al., 2017, 2016). However, they usually require special model architectures, undermining their practical applicability.

Distance to decision boundaries in deep learning. Decision boundaries of deep neural networks have been studied in various contexts. For example, some works explore the geometric properties of deep neural networks either in the input space (Fawzi et al., 2018; Karimi et al., 2019; Montufar et al., 2014; Poole et al., 2016) or in the weight space (Chaudhari et al., 2019; Choromanska et al., 2015; Dauphin et al., 2014; Dinh et al., 2017; Freeman and Bruna, 2016). Some works apply the properties of decision boundaries to address practical questions, such as adversarial defense (Croce and Hein, 2020; He et al., 2018; Heo et al., 2019), OOD detection (Lee et al., 2020), and domain generalization (Li et al., 2022; Yousefzadeh, 2021). Similar to Li et al. (2018), MANO discusses the distance between the learned intermediate feature to each decision boundary in the last hidden space.

Normalization in deep learning. Normalization is a crucial technique extensively utilized across various fields in deep learning, including domain generalization (Fan et al., 2021; Seo et al., 2020; Wang et al., 2021), metric learning (Oord et al., 2018; Sohn, 2016; Wu et al., 2018), face recognition (Deng et al., 2019; Liu et al., 2017; Ranjan et al., 2017; Wang et al., 2017; Zhang et al., 2019) and self-supervised learning (Chen et al., 2020). For example, TENT (Wang et al., 2021) normalizes features of test data using the mean value and standard deviation estimated from the target data. L_2 -constrained softmax (Ranjan et al., 2017) introduces L_2 normalization on features. These

normalization techniques are primarily employed to adapt new samples to familiar domains, calculate similarity, and speed up convergence. However, our proposed normalization focuses on reducing the negative implications of poorly calibrated scenarios.

C Background on Tsallis Entropies

The definition of Tsallis α -entropies (Tsallis, 1988) is given below.

Definition C.1 (Tsallis α -entropies). *Let $\mathbf{p} \in \Delta_K$ be a probability distribution. Let $\alpha > 1$ and $k \geq 0$. The Tsallis α -entropy is defined as:*

$$\mathbf{H}_\alpha^T(\mathbf{p}) = k(\alpha - 1)^{-1}(1 - \|\mathbf{p}\|_\alpha^\alpha).$$

It is common to take $k = 1$ or $k = \frac{1}{\alpha}$ following Blondel et al. (2019). The Tsallis α -entropy generalizes the Boltzmann-Gibbs theory of statistic mechanics to nonextensive systems. It has been used as a measure of disorder and uncertainty in many applications (Gell-Mann and Tsallis, 2004; Negrinho and Martins, 2014; Sneddon, 2007; Teimoori et al., 2024), including in Machine Learning (Blondel et al., 2019, 2020; Muzellec et al., 2017). Moreover, they generalize two widely-known measures of uncertainty. Indeed, the limit case $\alpha \rightarrow 1$ leads to the Shannon entropy \mathbf{H}_S (see Peters et al., 2019, Appendix A.1), *i.e.*, $\lim_{\alpha \rightarrow 1} \mathbf{H}_\alpha^T(\mathbf{p}) = \mathbf{H}_S(\mathbf{p}) = -\sum_{j=1}^K p_j \ln(p_j)$, while taking $\alpha = 2$ leads to the Gini index \mathbf{G} , a popular impurity measure for decision trees (Gini, 1912), *i.e.*, $\mathbf{H}_2^T(\mathbf{p}) = \frac{1}{2}(1 - \|\mathbf{p}\|_2^2) = \mathbf{G}(\mathbf{p})$. Tsallis entropies measure the uncertainty: the higher the entropy the greater the uncertainty. From a probabilistic perspective, the entropy will take high values for *uncertain* probability distributions, *i.e.*, close to the uniform distribution. We visualize the evolution of the Tsallis entropy for varying parameters α in Figure 6, where the case $\alpha = 1$ corresponds to the Shannon entropy.

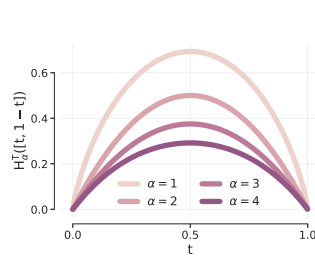


Figure 6: Tsallis α -entropies of $[t, 1 - t]$ for $t \in [0, 1]$.

D Theoretical Insights and Proofs

In this section, we provide theoretical insights for Section 4 and the proofs of our theoretical results.

Notations. Scalar values are denoted by regular letters (e.g., parameter λ), vectors are represented in bold lowercase letters (e.g., vector \mathbf{x}) and matrices are represented by bold capital letters (e.g., matrix \mathbf{A}). The i -th row of the matrix \mathbf{A} is denoted by \mathbf{A}_i , its j -th column is denoted by $\mathbf{A}_{\cdot,j}$ and its elements are denoted by $\mathbf{A}_{i,j}$. The trace of a matrix \mathbf{A} is denoted by $\text{Tr}(\mathbf{A})$ and its transpose by \mathbf{A}^\top . The L_p norm of a vector \mathbf{x} is denoted by $\|\mathbf{x}\|_p$, and by abuse of notation we denote it by $\|\mathbf{A}\|_p$ for a matrix \mathbf{A} with $\|\mathbf{A}\|_p^p = \sum_i \|\mathbf{A}_i\|_p^p = \sum_{i,j} |\mathbf{A}_{i,j}|^p$. Let $\Delta_K := \{\mathbf{p} \in [0, 1]^K \mid \sum_{i=1}^K p_i = 1\}$ be the K -dimensional probability simplex.

D.1 Impact of Prediction Errors

Let $\mathbf{x} \in \mathcal{D}_{\text{test}}$ be a test sample with ground-truth label $y \in \{1, \dots, K\}$. In multi-class classification, the softmax operator is used to approximate the posterior probability $p(y|\mathbf{x})$ (see Bishop, 2006, chap.4, p.198). Reusing the notations of Section 4, because of the distribution shifts between source and target, logits are subject to a prediction bias $\varepsilon = (\varepsilon_k)_k$ and write $f(\mathbf{x}) = \mathbf{q}^* + \varepsilon$ where \mathbf{q}^* are ground-truth logits. In this section, we study the impact of such bias on the approximation of the posterior $p(y|\mathbf{x})$.

Impact on the posterior approximation. Proposition 3.1 shows the impact of the prediction bias on the KL divergence between the true class posterior probabilities, assumed modeled as $\mathbf{p} = \text{softmax}(\mathbf{q}^*) \in \Delta_K$, and the estimated ones $\mathbf{s} = \text{softmax}(f(\mathbf{x})) \in \Delta_K$. In particular, it states that

$$0 \leq \text{KL}(\mathbf{p}||\mathbf{s}) \leq \varepsilon_+^T \mathbf{p}, \quad (7)$$

where $\varepsilon_+ = (\max_l \{\varepsilon_l\} - \varepsilon_k)_k \in \mathbb{R}_+^K$. The proof is given below.

Proof. We denote $\mathbf{q} = f(\mathbf{x}) \in \mathbb{R}^K$ the neural network's outputs on a given test sample \mathbf{x} . We first remark that

$$\begin{aligned} \text{KL}(\mathbf{p}||\mathbf{s}) &= \sum_k \mathbf{p}_k \ln \left(\frac{\mathbf{p}_k}{\mathbf{s}_k} \right) \\ &= \sum_k \mathbf{p}_k \ln \left(\frac{\exp(\mathbf{q}_k^*)}{\sum_{j=1}^K \exp(\mathbf{q}_j^*)} \cdot \frac{\sum_{j=1}^K \exp(\mathbf{q}_j^* + \varepsilon_j)}{\exp(\mathbf{q}_k^* + \varepsilon_k)} \right) \\ &= \sum_k \mathbf{p}_k \ln \left(\exp(-\varepsilon_k) \cdot \frac{\sum_{j=1}^K \exp(\mathbf{q}_j^* + \varepsilon_j)}{\sum_{j=1}^K \exp(\mathbf{q}_j^*)} \right). \end{aligned} \quad (8)$$

To obtain the upper-bound, we notice that

$$\exp(\mathbf{q}_j^* + \varepsilon_j) = \exp(\mathbf{q}_j^*) \exp(\varepsilon_j) \leq \exp(\mathbf{q}_j^*) \cdot \max_l \{\exp(\varepsilon_l)\}.$$

This leads to

$$\frac{\sum_{j=1}^K \exp(\mathbf{q}_j^* + \varepsilon_j)}{\sum_{j=1}^K \exp(\mathbf{q}_j^*)} \leq \frac{\max_l \{\exp(\varepsilon_l)\} \sum_{j=1}^K \exp(\mathbf{q}_j^*)}{\sum_{j=1}^K \exp(\mathbf{q}_j^*)} = \max_l \{\exp(\varepsilon_l)\}. \quad (9)$$

Using the fact that all the terms are positive and that \ln and \exp are increasing functions, we obtain from Eq. (8) that

$$\begin{aligned} \sum_k \mathbf{p}_k \ln \left(\exp(-\varepsilon_k) \cdot \frac{\sum_{j=1}^K \exp(\mathbf{q}_j^* + \varepsilon_j)}{\sum_{j=1}^K \exp(\mathbf{q}_j^*)} \right) &\leq \sum_k \mathbf{p}_k \ln(\exp(-\varepsilon_k) \cdot \max_l \{\exp(\varepsilon_l)\}) \\ &\leq \sum_k \mathbf{p}_k [\ln(\exp(\max_l \{\varepsilon_l\})) - \varepsilon_k] \\ &\leq \sum_k \mathbf{p}_k [\max_l \{\varepsilon_l\} - \varepsilon_k] \\ &= \varepsilon_+^T \mathbf{p}. \end{aligned} \quad (10)$$

Combining Eq. (8) and Eq. (10) gives the upper bound. \square

The quantities ε_+ is a linear transformation of the prediction bias $\varepsilon \in \mathbb{R}^K$ and has nonnegative entries, which means each class is overestimated, representing an *overconfident* model. Proposition 3.1 shows that the discrepancy between the error approximation of the posterior probabilities is controlled by the alignment between the posterior and this extreme prediction bias. In addition, by a simple application of Cauchy-Schwartz in Eq. (7) and using the fact that $\|\mathbf{p}\| = \sum_{k=1}^K \mathbf{p}_k^2 \leq \sum_{k=1}^K \mathbf{p}_k = 1$, we have $\text{KL}(\mathbf{p}||\mathbf{s}) \leq \|\varepsilon_+\|_2$. In particular, in the perfect situation where $\varepsilon = \mathbf{0}$, ε_+ is equal to 0 and the softmax probabilities perfectly approximate the posterior. In summary, Proposition 3.1 indicates that not only the norm of the prediction bias but also its alignment to the posterior is responsible for the approximation error of the posterior. In our setting, it means that logits-methods need a low prediction bias on classes on which the model is confident such that softmax probabilities can be reliably used to estimate accuracy. This follows our analysis and empirical verification from Section 4.

A real-world example. Although we usually tend to think that a high prediction bias shifts the predicted posterior towards the uniform distribution, in the general case, other situations may happen that hinder the quality of the accuracy estimation. For example, one may think of a letter recognition task with a neural network pre-trained on the Latin alphabet and tested on the Cyrillic one. In this case, some prediction probabilities will be adversarial as the neural network will not be aware of the semantic differences between the Latin ‘‘B’’ and the Cyrillic ‘‘B’’, therefore predicting a wrong class with high probability.

D.2 Choice of Threshold $\Phi(\mathcal{D}_{\text{test}})$ in Eq. (6)

To automatically select the appropriate normalization function in MANO (Algorithm 1), we introduced a decision threshold $\Phi(\mathcal{D}_{\text{test}})$ equal, up to a constant, to the average KL divergence between the uniform distribution and the predicted softmax probabilities. This stems from Tian et al. (2021) that showed that this KL divergence was a measure of the model’s uncertainty. In this section, we provide theoretical insights into this formulation by establishing the connection between $\Phi(\mathcal{D}_{\text{test}})$ and the misclassification error made on the test data. We first introduce the following lemma that is inspired from Lemma 4 in Seldin and Tishby (2010).

Lemma D.1 (Change of measure inequality (Seldin and Tishby, 2010)). *Let Z be a random variable on $\{1, \dots, K\}$ and $\boldsymbol{\mu} = (\mu_k)_k \in \Delta_K$ and $\boldsymbol{\nu} = (\nu_k)_k \in \Delta_K$ be two probability distributions. For any measurable function $\psi: \mathcal{Z} \rightarrow \mathbb{R}$, the following inequality holds:*

$$\sum_{k=1}^K \mu_k \psi(k) \leq \text{KL}(\boldsymbol{\mu} \parallel \boldsymbol{\nu}) + \ln \left(\sum_{k=1}^K \nu_k \exp(\psi(k)) \right).$$

Proof. We have

$$\begin{aligned} \sum_{k=1}^K \mu_k \psi(k) &= \sum_{k=1}^K \mu_k \ln \left(\frac{\mu_k}{\nu_k} \exp(\psi(k)) \frac{\nu_k}{\mu_k} \right) \\ &= \sum_{k=1}^K \mu_k \ln \left(\frac{\mu_k}{\nu_k} \right) + \sum_{k=1}^K \mu_k \ln \left(\exp(\psi(k)) \frac{\nu_k}{\mu_k} \right) \\ &= \text{KL}(\boldsymbol{\mu} \parallel \boldsymbol{\nu}) + \sum_{k=1}^K \mu_k \ln \left(\exp(\psi(k)) \frac{\nu_k}{\mu_k} \right) \quad (\text{Definition of } \text{KL}(\cdot \parallel \cdot)) \\ &\leq \text{KL}(\boldsymbol{\mu} \parallel \boldsymbol{\nu}) + \ln \left(\sum_{k=1}^K \mu_k \exp(\psi(k)) \frac{\nu_k}{\mu_k} \right) \quad (\text{Jensen inequality}) \\ &= \text{KL}(\boldsymbol{\mu} \parallel \boldsymbol{\nu}) + \ln \left(\sum_{k=1}^K \nu_k \exp(\psi(k)) \right). \end{aligned}$$

□

Let $\mathbf{u} = \frac{1}{K} \mathbb{1}_K \in \Delta_K$ be the uniform probability. The test dataset writes $\mathcal{D}_{\text{test}} = \{\mathbf{x}_i\}_{i=1}^N$ with corresponding logits $\mathbf{q}_i = f(\mathbf{x}_i)$ and ground-truth labels $\mathcal{Y}_{\text{test}} = \{y_i\}_{i=1}^N$ (unavailable in practice). We denote the softmax probabilities by $\mathbf{s}^i = \text{softmax}(\mathbf{q}_i) = \exp(\mathbf{q}_i) / \sum_{k=1}^K \exp(\mathbf{q}_i)_k \in \Delta_K$. We introduce the entropy of a probability vector as $H(\mathbf{p}) = -\frac{1}{K} \sum_{k=1}^K \mathbf{p}_k \ln(\mathbf{p}_k)$. In particular, it is a measure of uncertainty and takes a high value on uncertain probabilities, *i.e.*, close to the uniform. We establish in the following proposition the connection between the criterion $\Phi(\mathcal{D}_{\text{test}})$, the miscalibration error, the model’s confidence, and its entropy.

Proposition D.2 ($\Phi(\mathcal{D}_{\text{test}})$, misclassification error, confidence and entropy). *We have*

$$\underbrace{\xi(\mathcal{D}_{\text{test}}, \mathcal{Y}_{\text{test}})}_{\text{misclassification}} + \underbrace{\mathcal{U}(\mathcal{D}_{\text{test}})}_{\text{confidence}} + \underbrace{\mathcal{H}(\mathcal{D}_{\text{test}})}_{\text{entropy}} \leq \underbrace{\Phi(\mathcal{D}_{\text{test}})}_{\text{criterion}} + \ln \left(e + \frac{1}{K} \right),$$

where $\xi(\mathcal{D}_{\text{test}}, \mathcal{Y}_{\text{test}}) = \frac{1}{N} \sum_{i=1}^N (1 - s_{y_i}^i)$, $\mathcal{U}(\mathcal{D}_{\text{test}}) = \frac{1}{N} \sum_{i=1}^N \text{KL}(\mathbf{u} \parallel \mathbf{s}^i)$, and $\mathcal{H}(\mathcal{D}_{\text{test}}) = \frac{1}{N} \sum_{i=1}^N H(\mathbf{s}^i)$.

Proof. For a given test sample $\mathbf{x}_i \in \mathcal{D}_{\text{test}}$, we first notice that

$$\text{KL}(\mathbf{u} \parallel \mathbf{s}^i) = \sum_{k=1}^K \mathbf{u}_k \ln\left(\frac{\mathbf{u}_k}{\mathbf{s}_k^i}\right) = \frac{1}{K} \sum_{k=1}^K \ln\left(\frac{1}{K}\right) - \ln(\mathbf{s}_k^i) = -\ln(K) - \frac{1}{K} \sum_{k=1}^K \ln(\mathbf{s}_k^i).$$

Similarly, we obtain $\text{KL}(\mathbf{s}^i \parallel \mathbf{u}) = \sum_{k=1}^K \mathbf{s}_k^i \ln(\mathbf{s}_k^i) + \ln(K)$. Combining those results leads to

$$\begin{aligned} \text{KL}(\mathbf{u} \parallel \mathbf{s}^i) + \text{KL}(\mathbf{s}^i \parallel \mathbf{u}) &= -\frac{1}{K} \sum_{k=1}^K \ln(\mathbf{s}_k^i) + \sum_{k=1}^K \mathbf{s}_k^i \ln(\mathbf{s}_k^i) \\ \iff \text{KL}(\mathbf{s}^i \parallel \mathbf{u}) &= -\text{KL}(\mathbf{u} \parallel \mathbf{s}^i) - \frac{1}{K} \sum_{k=1}^K \ln(\mathbf{s}_k^i) + \sum_{k=1}^K \mathbf{s}_k^i \ln(\mathbf{s}_k^i). \end{aligned}$$

Consider the function $\psi(k) = \mathbb{I}(y_i \neq k)$ that takes the value 1 when $y_i \neq k$ and 0 otherwise. Using Lemma D.1 with the measures $\boldsymbol{\mu} = \mathbf{s}^i$, $\boldsymbol{\nu} = \mathbf{u}$ and ψ , and the previous equation, we obtain

$$\begin{aligned} \sum_{k=1}^K \mathbf{s}_k^i \mathbb{I}(y_i \neq k) &\leq +\text{KL}(\mathbf{s}^i \parallel \mathbf{u}) + \ln\left(\sum_{k=1}^K \mathbf{u}_k \exp(\mathbb{I}(y_i \neq k))\right) \\ \iff \sum_{k=1}^K \mathbf{s}_k^i \mathbb{I}(y_i \neq k) &\leq -\text{KL}(\mathbf{u} \parallel \mathbf{s}^i) - \frac{1}{K} \sum_{k=1}^K \ln(\mathbf{s}_k^i) + \sum_{k=1}^K \mathbf{s}_k^i \ln(\mathbf{s}_k^i) + \ln\left(\sum_{k=1}^K \mathbf{u}_k \exp(\mathbb{I}(y_i \neq k))\right) \\ \iff 1 - \mathbf{s}_{y_i}^i &\leq -\text{KL}(\mathbf{u} \parallel \mathbf{s}^i) - \frac{1}{K} \sum_{k=1}^K \ln(\mathbf{s}_k^i) - \text{H}(\mathbf{s}^i) + \ln\left(\frac{1}{K}(Ke + 1)\right) \quad (\sum_{k=1}^K \mathbf{s}_k^i = 1) \\ \iff 1 - \mathbf{s}_{y_i}^i + \text{KL}(\mathbf{u} \parallel \mathbf{s}^i) + \text{H}(\mathbf{s}^i) &\leq -\frac{1}{K} \sum_{k=1}^K \ln(\mathbf{s}_k^i) + \ln\left(e + \frac{1}{K}\right). \end{aligned}$$

Summing over all the test samples and dividing by N leads to

$$\frac{1}{N} \sum_{i=1}^N (1 - \mathbf{s}_{y_i}^i) + \frac{1}{N} \sum_{i=1}^N \text{KL}(\mathbf{u} \parallel \mathbf{s}^i) + \frac{1}{N} \sum_{i=1}^N \text{H}(\mathbf{s}^i) \leq \underbrace{-\frac{1}{NK} \sum_{i=1}^N \sum_{k=1}^K \ln(\mathbf{s}_k^i)}_{=\Phi(\mathcal{D}_{\text{test}})} + \ln\left(e + \frac{1}{K}\right),$$

which concludes the proof by using the notations introduced in Proposition D.2. \square

Interpretation. The term $\xi(\mathcal{D}_{\text{test}}, \mathcal{Y}_{\text{test}})$, dubbed misclassification error, is the expected error on the test set between the optimal probability on the true label (*i.e.*, 1) and the predicted probability $\mathbf{s}_{y_i}^i$. It takes high values when the model makes a lot of mistakes and low values otherwise. $\mathcal{U}(\mathcal{D}_{\text{test}})$ is the expected KL divergence on the test set between the predicted probabilities and the uniform distribution and it measures the model's confidence (Tian et al., 2021). It takes high values when the predicted probabilities are far from the uniform (confidence) and low values when they are close to the uniform (uncertain). $\mathcal{H}(\mathcal{D}_{\text{test}})$ is the expected entropy on the test set of the predicted probabilities. It takes high values when predicted probabilities are close to the uniform and low values otherwise. Finally, $\Phi(\mathcal{D}_{\text{test}})$ is the criterion used in Eq. 6 to select the proper normalization function. Proposition D.2 implies $\Phi(\mathcal{D}_{\text{test}})$ can take *high values* in three situations (the case of few mistakes but an uncertain model is ignored as it rarely happens in practice on such a challenging task):

1. $\xi(\mathcal{D}_{\text{test}}, \mathcal{Y}_{\text{test}})$ is high, *i.e.*, the model makes a lot of mistakes while being confident so $\mathcal{U}(\mathcal{D}_{\text{test}})$ is high and $\mathcal{H}(\mathcal{D}_{\text{test}})$ is low;
2. $\xi(\mathcal{D}_{\text{test}}, \mathcal{Y}_{\text{test}})$ is high, *i.e.*, the model makes a lot of mistakes while being uncertain so $\mathcal{U}(\mathcal{D}_{\text{test}})$ is low and $\mathcal{H}(\mathcal{D}_{\text{test}})$ is low;
3. $\xi(\mathcal{D}_{\text{test}}, \mathcal{Y}_{\text{test}})$ is low, *i.e.*, the model makes few mistakes and is confident so $\mathcal{U}(\mathcal{D}_{\text{test}})$ is high and $\mathcal{H}(\mathcal{D}_{\text{test}})$ is low.

In the normalization strategy `SoftTrun` used in MANO, we assume that a high $\Phi(\mathcal{D}_{\text{test}})$ indicates that the model is confident, and vice-versa. Indeed, we consider that when $\Phi(\mathcal{D}_{\text{test}}) \leq \eta$, uncertainty

is high and we truncate the exponential to reduce error accumulation, while when $\Phi(\mathcal{D}_{\text{test}}) > \eta$, the model can be trusted and complete information is used with the exact exponential (and we recover the `softmax`). This corresponds to the last situation and follows the empirical evidence from [Tian et al. \(2021\)](#) that showed that this KL divergence was small when the uncertainty of the model was high and large for confident models. While this does not cover all the situations, we experimentally show the benefits of $\Phi(\mathcal{D}_{\text{test}})$ and `SoftTrun` in [Section 5](#) where MANO achieves superior performance against 11 commonly used baselines for various architectures and types of shifts on 12 datasets.

D.3 Choice of η in Eq. (6)

In all our experiments, we take $\eta = 5$ for the selection criterion in Eq. (6). We motivate this choice in what follows. In our setting, we consider test samples $\mathbf{x}_i \in \mathcal{D}_{\text{test}}$ drawn i.i.d. from the test distribution p_T . As the model f pre-trained on $\mathcal{D}_{\text{train}}$ is a deterministic function, the logits \mathbf{q}_i are i.i.d. random variables and the decision threshold $\Phi(\mathcal{D}_{\text{test}}) = -\frac{1}{NK} \sum_{i=1}^N \sum_{k=1}^K \ln \left(\frac{\exp(\mathbf{q}_i)_k}{\sum_{j=1}^K \exp(\mathbf{q}_i)_j} \right)$ is a random variable with mean μ and variance ν . Applying the Chebyshev’s inequality leads to

$$\mathbb{P}(|\Phi(\mathcal{D}_{\text{test}}) - \mu| > \nu\eta) \leq \frac{1}{\eta^2}. \quad (11)$$

The threshold $\Phi(\mathcal{D}_{\text{test}})$ is used to determine how calibrated the model is on a given test dataset $\mathcal{D}_{\text{test}}$. [Figure 2\(b\)](#) shows that our proposed normalization is optimal in poorly calibrated datasets and performs slightly below the `softmax` in calibrated situations. Hence, we can afford to be conservative and we want to consider the model calibrated only for *extreme* values of $\Phi(\mathcal{D}_{\text{test}})$. From Eq. (11), taking $\eta = 5$ ensures that the probability that $\Phi(\mathcal{D}_{\text{test}})$ deviates from its mean by several standard deviations with probability smaller than 5% ($\frac{1}{25} < 0.05$). It should be noted that we do not claim the optimality of this choice nor the optimality of our automatic selection in Eq. (6). However, it is particularly difficult to define decision rules in unsupervised and semi-supervised settings ([Amini et al., 2022](#)). Moreover, using Eq. (6), MANO remains suitable even when test labels are not available which is often the case in real-world applications, and we demonstrate state-of-the-art performance for various architecture and types of shifts in [Section 5](#).

D.4 Distance to the Hyperplane

Lemma D.3 ([Dohmatob \(2020\)](#)). *Let $\omega \in \mathbb{R}^n$ be non zero and $b \in \mathbb{R}$. The distance between any point $\mathbf{z} \in \mathbb{R}^n$ and the hyperplane $\{\mathbf{x} | \omega^\top \mathbf{x} + b = 0\}$ writes $d(\omega, \mathbf{z}) = |\omega^\top \mathbf{z} + b| / \|\omega\|$.*

Proof. The proof follows the geometric intuition from [Dohmatob \(2020\)](#). We recall it here for the sake of self-consistency. The distance between \mathbf{z} and the hyperplane $\mathcal{H} = \{\mathbf{x} \in \mathbb{R}^n | \omega^\top \mathbf{x} + b = 0\}$ is equal to the distance between \mathbf{z} and its orthogonal projection on \mathcal{H} . We consider the line $L = \{\mathbf{z} + t\omega | t \in \mathbb{R}\}$ that is orthogonal to \mathcal{H} and passes through \mathbf{z} . The desired orthogonal projection is simply the point $\mathbf{z} + t^*\omega$ such that L and \mathcal{H} intersects, *i.e.*, such that

$$\begin{aligned} \omega^\top (\mathbf{z} + t^*\omega) + b = 0 &\Leftrightarrow \omega^\top \mathbf{z} + b = -t^* \|\omega\|^2 \\ &\Leftrightarrow t^* = -\frac{\omega^\top \mathbf{z} + b}{\|\omega\|^2}. \end{aligned} \quad (\|\omega\| \neq 0)$$

It follows that the distance between \mathbf{z} and \mathcal{H} writes

$$d(\omega, \mathbf{z}) = \|\mathbf{z} - \mathbf{z} + t^*\omega\| = \left\| -\frac{\omega^\top \mathbf{z} + b}{\|\omega\|^2} \times \omega \right\| = \frac{|\omega^\top \mathbf{z} + b|}{\|\omega\|}.$$

□

D.5 Proof of Theorem 3.3

Proof. Reusing the notations introduced in Section 3.2 and Algorithm 1, we have that

$$\begin{aligned}
\mathcal{S}(f, \mathcal{D}_{\text{test}})^p &= \frac{1}{NK} \|\mathbf{Q}\|_p^p = \frac{1}{NK} \sum_{i=1}^N \|\mathbf{Q}_i\|_p^p && \text{(Definition of } \|\mathbf{Q}\|_p \text{)} \\
&= \frac{1}{NK} \sum_{i=1}^N \|\sigma(\mathbf{q}_i)\|_p^p && \text{(Definition of } \mathbf{Q}_i \text{ in Algorithm 1)} \\
&= \frac{1}{NK} \sum_{i=1}^N 1 - (1 - \|\sigma(\mathbf{q}_i)\|_p^p) \\
&= \frac{1}{K} - \frac{p(p-1)}{NK} \sum_{i=1}^N \frac{1}{p(p-1)} (1 - \|\sigma(\mathbf{q}_i)\|_p^p) \\
&= \frac{1}{K} - \frac{p(p-1)}{NK} \sum_{i=1}^N \mathbf{H}_p^T(\sigma(\mathbf{q}_i)) && \text{(Definition of } \mathbf{H}_p^T \text{)} \\
&= b - a \left(\frac{1}{N} \sum_{i=1}^N \mathbf{H}_p^T(\sigma(\mathbf{q}_i)) \right),
\end{aligned}$$

where $a = \frac{p(p-1)}{K} > 0$ and $b = \frac{1}{K}$. Rearranging the terms concludes the proof. \square

D.6 Properties of ϕ

The softmax can be decomposed as $\text{softmax}(\mathbf{q}) = \exp(\mathbf{q}) / \sum_{k=1}^K \exp(\mathbf{q})_k = (\phi \circ \exp)(\mathbf{q})$, where $\phi: \mathbb{R}_+^K \rightarrow \Delta_K$ writes $\phi(\mathbf{u}) = \mathbf{u} / \sum_{k=1}^K \mathbf{u}_k = \mathbf{u} / \|\mathbf{u}\|_1$. We extend the domain of ϕ to \mathbb{R}_+^K by setting $\phi(\mathbf{0}) = \frac{1}{K} \mathbb{1}_K$. The following proposition states the properties of ϕ .

Proposition D.4 (Properties of ϕ).

1. **Generalized injectivity.** $\forall \mathbf{u}, \mathbf{v} \in \mathbb{R}_+^K \setminus \{\mathbf{0}\}$, $\phi(\mathbf{u}) = \phi(\mathbf{v}) \iff \exists \alpha \in \mathbb{R}^*$, s.t. $\mathbf{u} = \alpha \mathbf{v}$
2. **Evaluation on constant inputs.** Let $\mathbf{u} = \alpha \mathbb{1}_K$ with $\alpha \geq 0$. Then, we have $\phi(\mathbf{u}) = \frac{1}{K} \mathbb{1}_K$.

Proof. We start by proving the first part of Proposition D.4. Let $\mathbf{u}, \mathbf{v} \in \mathbb{R}_+^K \setminus \mathbf{0}$. We have

$$\phi(\mathbf{u}) = \phi(\mathbf{v}) \iff \frac{\mathbf{u}}{\|\mathbf{u}\|_1} = \frac{\mathbf{v}}{\|\mathbf{v}\|_1} \iff \mathbf{u} = \underbrace{\frac{\|\mathbf{u}\|_1}{\|\mathbf{v}\|_1}}_{\alpha > 0} \times \mathbf{v}.$$

Then, we prove the second part of the proposition. Let $\alpha \geq 0$ and consider $\mathbf{u} = \alpha \mathbb{1}_K \in \mathbb{R}_+^K$. If $\alpha = 0$, then $\mathbf{u} = \mathbf{0}$ and by definition, $\phi(\mathbf{u}) = \phi(\mathbf{0}) = \frac{1}{K} \mathbb{1}_K$. Assuming $\alpha > 0$, we have

$$\phi(\mathbf{u}) = \frac{\mathbf{u}}{\|\mathbf{u}\|_1} = \frac{\mathbf{u}}{\sum_{k=1}^K \mathbf{u}_k} = \frac{\alpha}{\sum_{k=1}^K \alpha} \times \mathbb{1}_K = \frac{1}{K} \mathbb{1}_K.$$

\square

The first part of the proposition is dubbed ‘‘generalized injectivity’’ as the injectivity can be retrieved by fixing $\alpha = 1$ in Proposition D.4. It ensures that ϕ only has *equal* outputs if the inputs are *similar*. To illustrate that, consider the logits $\mathbf{q}, \delta \in \mathbb{R}^K$. From Proposition D.4, having $\text{softmax}(\mathbf{q}) = \text{softmax}(\delta)$ is equivalent to having $\exp(\mathbf{q}) = \alpha \exp(\delta)$ for some $\alpha \neq 0$. By positivity of both sides, it implies $\alpha > 0$, and taking the logarithm leads to $\mathbf{q} = \delta + \ln \alpha$. It means that \mathbf{q} is equal to δ up to a

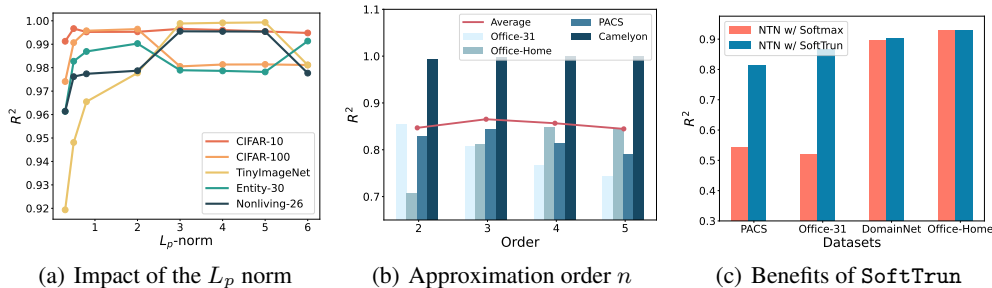


Figure 7: **Sensitivity analysis with Resnet18.** (a) Effect of the L_p norm types. (b) Impact of the Taylor approximation order, *i.e.*, the number of terms in Eq 4. For instance, an order of 3 means that 3 terms are taken, which corresponds to the default setting in Eq. (6) and is used in all our experiments. (c) Type of normalization function.

fixed constant. From a learning perspective, those logits will thus have the same predicted label and the same normalized logits. Proposition D.4 shows that using ϕ preserves the information from the neural network. In addition, if the neural network’s output is not informative, *i.e.*, all entries are equal, then the link function gives equal probability to all classes.

E Sensitivity Analysis and Ablation Study

E.1 Choice of L_p Norm.

To reflect the impact of different L_p norms on estimation performance, we conduct a sensitivity study on 5 datasets with ResNet18, whose results are shown in Figure 7(a). The performance for $p = 1$ is ignored as in this case, $\|\mathbf{Q}\|_1 = 1$ because \mathbf{Q} is right-stochastic. We can see that when we choose $p \in [2, 5]$, the results fluctuate within a satisfying range. This can be explained by the fact that within this range, we emphasize adequately the large positive feature-to-boundary distances without ignoring the other comparatively small distances.

E.2 Choice of Taylor Approximation order.

In Figure 7(b), we verify the impact of Taylor formula approximation on final accuracy estimation performance. It should be noted that for orders higher than in the default setting in Eq. (6), the positivity is lost. To alleviate this issue, we consistently remove for all orders the minimum value of the obtained vector to each of its entries to ensure having an output in \mathbb{R}_+^K . This extends de Brébisson and Vincent (2016) to orders higher than 2. From this figure, we can see that when we reserve the first three terms in the Taylor formula, the average estimation performance is optimal. For well-calibrated datasets such as Office-Home and WILDS, there exists an increased trend of estimation performance when we reserve more Taylor formula terms. As for suboptimal-calibrated datasets such as PACS and Office-31, their performance rises when fewer terms are reserved. It empirically certifies that the normalization technique is a trade-off tool between the ground-truth logits’ information and error accumulation. In addition, the optimal choice is to keep 3 terms in Eq. (4) which motivates our default setting in Eq (6).

E.3 Superiority of SoftTrun.

To verify the effectiveness of our proposed normalization technique, SoftTrun, we conduct an ablation study by replacing our normalization with the softmax function under the natural shift. In Figure 7(c), we observe that our proposed normalization significantly enhances the estimation performance of datasets from the natural shift. Especially, R^2 for poorly-calibrated datasets such as Office-31 is improved from 0.51 to 0.86.

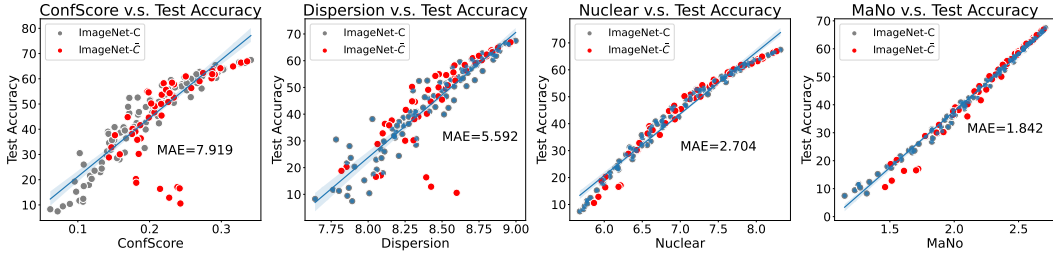


Figure 8: Comparison of generalization capability across four methods. Each subplot shows a linear regression model fitted on ImageNet-C to predict accuracy on ImageNet- \bar{C} . Mean absolute error (MAE) is calculated on ImageNet- \bar{C} (Mintun et al., 2021). All experiments use ResNet18.

E.4 Generalization Capabilities of MANO on ImageNet- \bar{C}

To further demonstrate the generalization capability of MANO, we provide a similar experiment with that in Section 5.3 on ImageNet-C and ImageNet- \bar{C} (Mintun et al., 2021) in Figure 8. In particular, we fit a linear regression function on ImageNet-C and use the linear function to predict the accuracy of ImageNet- \bar{C} . This figure shows that MANO has better estimation performance than the other baselines when meeting different corruption types.